

Direct simulation of a self-similar turbulent mixing layer

Michael M. Rogers and Robert D. Moser
NASA-Ames Research Center, Moffett Field, California 94035

(Received 9 March 1993; accepted 20 October 1993)

Three direct numerical simulations of incompressible turbulent plane mixing layers have been performed. All the simulations were initialized with the same two velocity fields obtained from a direct numerical simulation of a turbulent boundary layer with a momentum thickness Reynolds number of 300 computed by Spalart [J. Fluid Mech. **187**, 61 (1988)]. In addition to a baseline case with no additional disturbances, two simulations were begun with two-dimensional disturbances of varying strength in addition to the boundary layer turbulence. After a development stage, the baseline case and the case with weaker additional two-dimensional disturbances evolve self-similarly, reaching visual thickness Reynolds numbers of up to 20 000. This self-similar period is characterized by a lack of large-scale organized pairings, a lack of streamwise vortices in the "braid" regions, and scalar mixing that is characterized by "marching" probability density functions (PDFs). The case begun with strong additional two-dimensional disturbances only becomes approximately self-similar, but exhibits sustained organized large-scale pairings, clearly defined braid regions with streamwise vortices that span them, and scalar PDFs that are "nonmarching." It is also characterized by much more intense vertical velocity fluctuations than the other two cases. The statistics and structures in several experiments involving turbulent mixing layers are in better agreement with those of the simulations that do not exhibit organized pairings.

I. INTRODUCTION

There have been several experimental measurements of the statistics of high-Reynolds-number self-similar turbulent mixing layers (e.g., Refs. 1–5). They were performed with vorticity thickness Reynolds numbers (Re_ω) as high as 130 000 (Ref. 1) and with varying velocity ratios (U_l/U_h , where U_h and U_l are the high- and low-speed free-stream velocities, respectively). Unfortunately, there is a large variation among the experiments in even the most basic statistical quantities, like the normalized growth rate and the turbulence intensities. The normalized growth rate of the vorticity thickness (r_ω) is defined here as

$$r_\omega = \frac{U_h + U_l}{2(U_h - U_l)} \frac{d\delta_\omega}{dx} = \frac{U_c}{\Delta U} \frac{d\delta_\omega}{dx}, \quad (1)$$

where δ_ω is the vorticity thickness, ΔU is the velocity difference, and U_c is the convection velocity. This is the standard normalization used to eliminate the effect of different velocity ratios (e.g., Refs. 6–8). In the experiments cited above, r_ω varies from 0.081 in Liepmann and Laufer¹ to 0.098 in Wygnanski and Fiedler.² Furthermore, values of the maximum cross-stream velocity variance (normalized by ΔU^2) vary from 0.01 in Liepmann and Laufer¹ to 0.02 in Batt.⁴ Dimotakis and Brown⁹ suggested that the reason for these and other variations in experimental observations may be that turbulent mixing layers only slowly "forget" the details of their initial conditions. Mixing layers may thus exhibit a variety of apparently self-similar behaviors, which change very slowly.

Since Brown and Roshko's⁸ discovery of large-scale, apparently two-dimensional, structures in turbulent mixing

layers, there has been considerable research aimed at determining the origin, universality, and dynamical significance of these structures (see Ref. 10 for a review). The structures appear to be related to the two-dimensional rollers that form due to the instability of a laminar shear layer, and it has been widely assumed that these turbulent coherent structures will behave in the same way as their pretransition counterparts. However, it has also been suggested that two-dimensional turbulent rollers are not a universal feature of mixing layers, and that "pairings" can occur locally along the span of a roller.¹¹ Such "local pairings" have also been observed in transitional mixing layers.^{12,13,14} Thus the large-scale structures must depend on the character of the inlet disturbances, which may be facility dependent. Also, the dominance of the coherent structures in self-preserving turbulent mixing layers has been questioned by Hussain,¹⁵ who suggested that incoherent turbulence and coherent structures are comparably important in the dynamics of the layer.

The assumption that the turbulent rollers are dynamically similar to their nonturbulent counterparts is attractive because much is already known about laminar rollers and their instabilities. In particular, it is known that an array of such rollers is unstable to subharmonic disturbances, which lead to pairing,^{16,17} and indeed pairings have been reported in turbulent mixing layers. It is also known that the rollers are unstable to three-dimensional disturbances that result in their bending and the formation of the so-called rib vortices in the braid regions between the rollers.^{17,18} Recent results¹⁹ suggest that this three-dimensional instability is governed by two interacting mechanisms, one characteristic of flows dominated by ro-

tation (as in the roller), which leads to the bending of the roller, and the other associated with strain-dominated flows (as in the braid or saddle region), which leads to the formation of the rib vortices. As pointed out by Rogers and Moser,¹⁹ the magnitude of the strain in the braids and rollers of the two-dimensional rolled-up mixing layer is about the same at the centerline, so the difference in character between the two regions is caused by the reduced levels of spanwise vorticity in the braid region. Thus, if the turbulent rollers lead to braid regions that are substantially depleted of spanwise vorticity, we might expect rib vortices to form in the turbulent flow as well. There is experimental evidence for rib vortices in turbulent mixing layers (e.g., Refs. 20–22). However, it is not clear under what circumstances the laminar stability ideas discussed above are applicable to turbulent mixing layers.

It has become customary to examine the probability density function (PDF) of a passive scalar at various locations across the layer in an effort to quantify the character of the mixing (e.g., Refs. 4 and 23–27). Such PDFs have been observed to fall into two classes: marching PDFs, in which the most probable value of the scalar varies across the layer, with the most probable value on each side of the layer being closer to the free-stream value of that side, and nonmarching PDFs, in which the most probable value of the scalar is substantially independent of the position in the layer (and is determined by the entrainment ratio). Batt observed marching PDFs in a mixing layer in air at $Re_\omega \approx 40\,000$. On the other hand, Konrad found nonmarching behavior in his layer at $Re_\omega \approx 20\,000$ (in gas). In later experiments, Mungal and Dimotakis (in gas at $Re_\omega \approx 32\,000$) and Koochesfahani and Dimotakis (in water at $Re_\omega \approx 12\,000$) also found nonmarching PDFs and attributed the marching behavior observed by Batt to poor measurement resolution, although it seems unlikely that this could account entirely for the observed marching behavior. However, recent experimental measurements by Karasso and Mungal²⁸ with Re_ω up to 31 000 indicate that the ultimate state of a high-Reynolds-number turbulent mixing layer is characterized by marching PDFs.

To investigate the issues raised above, direct numerical simulations of turbulent mixing layers were performed. These simulations were designed to model experimental situations in which the splitter plate boundary layers are turbulent. Various statistical quantities are calculated and flow fields are examined for evidence of the large-scale rollers and other flow features that are expected by analogy with the structure in nonturbulent flows (i.e., spanwise rollers and streamwise rib vortices). In what follows, some preliminary issues are discussed in Sec. II, while Sec. III contains a description of the baseline simulation, and two simulations with slightly different initial conditions are presented in Sec. IV. Scalar mixing is examined in Sec. V, and discussion and conclusions are given in Sec. VI. Finally, the terms in the balance equations for the Reynolds stress components in the baseline flow are presented in the Appendix.

II. PRELIMINARIES

The numerical simulations discussed in this paper were performed by solving the three-dimensional time-dependent incompressible Navier–Stokes equations. For computational efficiency, a temporally evolving mixing layer was simulated rather than the spatially evolving layer typical of experiments. Comparisons of direct numerical simulations show that the temporally and spatially evolving mixing layers are qualitatively and in some cases quantitatively similar.²⁹ In this study, the solution domain is periodic in the streamwise (x_1) and spanwise (x_3) directions with periods $125\delta_m^0$ and $31.25\delta_m^0$, respectively, where δ_m^0 is the initial momentum thickness of the layer (defined below). Note that unlike the simulations performed by Rogers and Moser,^{19,30} the domain size is governed by the domain size of the boundary layer simulations from which the initial conditions were taken, rather than the expected wavelength of the mixing layer instability. The domain is infinite in the cross-stream (x_2) direction, and a Galerkin spectral method³¹ was used to solve the equations with as many as $512 \times 210 \times 192$ Fourier/Jacobi modes. A passive scalar with Schmidt number 1.0 that goes to zero and one in the free streams, is also simulated.

The momentum thickness of the mixing layer is defined by

$$\delta_m = \int_{-\infty}^{\infty} \left(\frac{1}{4} - \frac{\bar{U}_1^2}{\Delta U^2} \right) dx_2. \quad (2)$$

The initial momentum thickness δ_m^0 and the velocity difference ΔU are generally used for nondimensionalization, and the time-dependent momentum thickness is used as a measure of the layer thickness for the purpose of self-similar scaling, as in Ref. 1. Thus the self-similar cross-stream coordinate is defined to be $\xi = x_2/\delta_m(t)$. Momentum thickness is used for self-similar scaling rather than the vorticity thickness or other related scalings, which are more common in experiments, because the momentum thickness is less sensitive to statistical noise. This is because the momentum thickness is an integral quantity while the vorticity thickness is obtained from the derivative of the mean velocity. Consequently, the momentum thickness evolves smoothly in time while the vorticity thickness may not. During the self-similar development of the baseline flow discussed in Sec. III, the average ratio δ_ω/δ_m is 4.8. This ratio would be 4.44 or 4.00 if the mean profile were an error function or a hyperbolic tangent, respectively. Thus the ratio is sensitive to the detailed shape of the mean profile. In the following sections, experimental Reynolds numbers will be quoted based on either vorticity or momentum thickness, depending on context.

The initial conditions for the simulations described here were obtained from direct numerical simulations of a turbulent boundary layer with a momentum thickness of $0.75\delta_m^0$ computed by Spalart.³² Two different realizations of his simulation with a momentum thickness Reynolds number of 300 were used to mimic boundary layer turbulence on either side of the splitter plate in an experiment. To create a temporally evolving mixing layer, the two re-

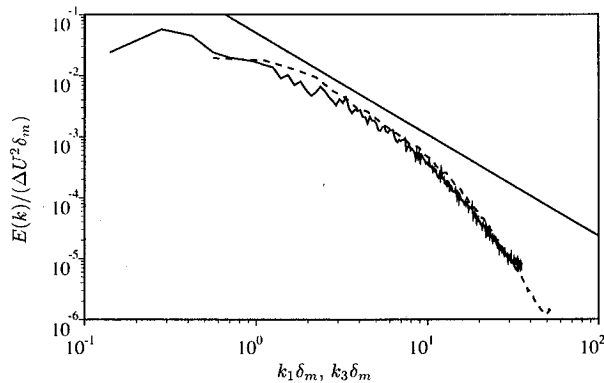


FIG. 1. One-dimensional energy ($u_i u_i$) density spectrum at the mixing layer centerline ($\tau = 170.5$). — vs k_1 , ---- vs k_3 .

alizations were brought together with their respective free streams moving in opposite directions. The situation is similar to a thin plate with boundary layers from oppositely moving flows on each side. At time zero, the plate is removed without disturbing the flow. The resulting mixing layer initially has a vorticity thickness Reynolds number, $Re_\omega = \Delta U \delta_\omega / \nu$, of 1370, and a momentum thickness Reynolds number, $Re_m = \Delta U \delta_m / \nu$ of 800. The layer Reynolds number grows as the layer spreads, with Re_ω and Re_m reaching 10 800 and 2420, respectively, by the end of the baseline simulation described in Sec. III. Another commonly quoted Reynolds number is that based on the “visual thickness,” which is unfortunately difficult to define precisely in the context of a simulation. A good approximation to the visual thickness is the vertical distance between the points where the mean product concentration of a fast chemical reaction is at 1% of its maximum value.²⁵ The Reynolds number based on this thickness ($Re_{1\%}$) reaches 20 000 by the end of the baseline simulation. Koochesfahani and Dimotakis²⁵ observed that the “mixing transition” in their experiments begun from laminar boundary layers occurred between $Re_{1\%} = 5600$ and $Re_{1\%} = 17\,000$. Furthermore, Breidenthal²⁰ found that the transition occurs at even lower Reynolds numbers as the velocity ratio approaches one (the limit in which the correspondence between temporally and spatially evolving mixing layers is exact). Thus the current simulations are at sufficiently high Reynolds number to produce fully developed turbulence.

Another indication of the high Reynolds numbers achieved in the simulations described here is the behavior of the energy spectra. One-dimensional energy spectra at the centerline of the baseline mixing layer described in Sec. III at $\tau = t \Delta U / \delta_m^0 = 170.5$ are shown in Fig. 1. The straight solid line has a slope of $-5/3$. The streamwise one-dimensional energy spectrum has approximately this slope over half a decade of variation in the streamwise wave number (k_1). Because of the limited spanwise domain size, a region of $-5/3$ slope is not as apparent in the spanwise (k_3) spectra.

III. THE BASELINE MIXING LAYER

The baseline simulation described in this section was initialized with two realizations of a turbulent boundary layer, as described in Sec. II. No added disturbances of any kind were used. In the following sections, this simulation will be referred to as the turbulent boundary layer (TBL) flow.

A. Statistics and self-similarity

It is well known that developed turbulent mixing layers evolve self-similarly,^{10,33} with a linearly growing thickness. By scaling large-scale quantities with the local layer thickness and the constant velocity difference, statistical profiles at different downstream locations (or at different times in the temporally evolving flow) collapse onto a single curve. In what follows, the numerically simulated mixing layer is examined for evidence of such self-similar evolution.

The evolution of the momentum thickness δ_m is shown in Fig. 2(a) as a function of the dimensionless time τ . Linear growth is achieved after $\tau \approx 70$. The integrated rate of dissipation of turbulent kinetic energy,

$$\mathcal{E} = \int_{-\infty}^{\infty} \epsilon \, dx_2 \quad (3)$$

($\epsilon = 2\nu \overline{S_{ij} S_{ij}}$, where S_{ij} is the strain-rate tensor) has units of velocity cubed and is thus nondimensionalized by ΔU^3 . Since ΔU is constant, \mathcal{E} should be constant when the layer is evolving self-similarly. The evolution of \mathcal{E} is also shown in Fig. 2(a). Shortly after $\tau \approx 100$, \mathcal{E} does become approximately constant until $\tau \approx 150$, after which a slight falloff occurs. This suggests that after $\tau \approx 150$ the self-similarity begins to break down. Other integrated large-scale statistics also evolve as expected for a self-similar layer over the period $105 < \tau < 150$. We thus identify this period as the period of self-similar evolution.

The mean velocity profiles at five times during the self-similar period are plotted with self-similar scaling in Fig. 2(b). Also included are the experimental data of Bell and Mehta⁵ for a mixing layer begun from turbulent (tripped) splitter-plate boundary layers with Re_m of up to 6000. (The experimental profiles have been shifted to center them at $x_2 = 0$, thus accounting for the drift of the center of the layer into the low-speed stream.) The collapse of the data at the five times is excellent, and the mean profile agrees very well with the data of Bell and Mehta. However, the collapse of the scaled mean profiles is not a sensitive indicator of self-similarity and is achieved for a longer time period from $\tau \approx 90$ to the end of the simulation at $\tau = 187.5$.

A more sensitive indicator of self-similarity is the collapse of the Reynolds stress profiles $\overline{u_i u_j}$ and the profiles of the components of the vorticity tensor $\overline{\omega_i \omega_j}$. The appropriate self-similar scaling for the Reynolds stresses is clear (ΔU^2); however, the appropriate scaling for the vorticity statistics is not as obvious. The required scaling can be determined by recalling that \mathcal{E} scales with ΔU^3 . In a mixing layer that is homogeneous in x_1 and x_3 we have the identity

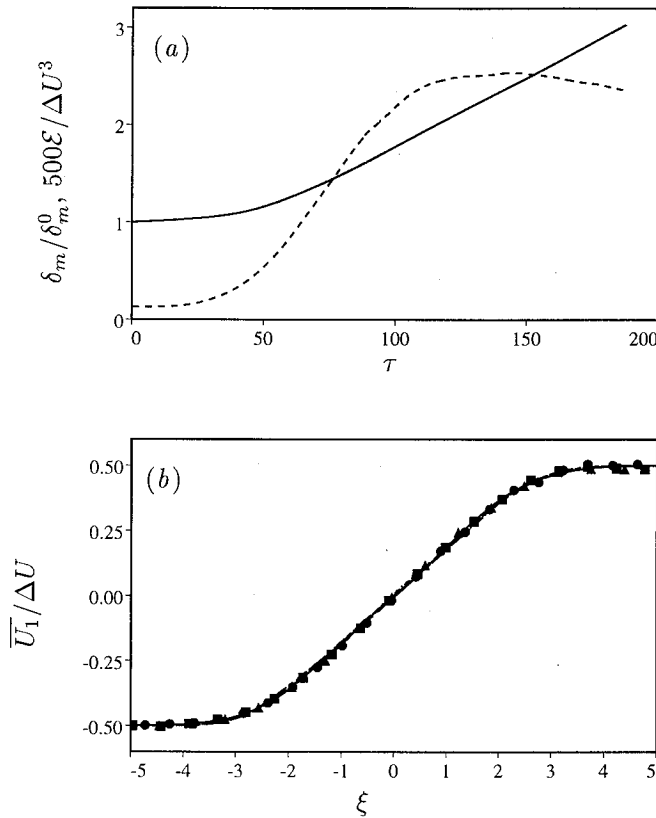


FIG. 2. Evidence of self-similarity. (a) Time evolution of δ_m/δ_m^0 and $500\mathcal{E}/\Delta U^3$. (b) Collapse of the mean velocity profiles $\bar{U}_1/\Delta U$ vs ξ at five times in the self-similar period (—: $\tau=105.2$, ---: $\tau=116.7$, ····: $\tau=128.6$, -·-·: $\tau=141.0$, - - - : $\tau=150.8$) compared with the experimental data of Bell and Mehta (1990) at three downstream locations (\blacksquare , $x_1=108.1$ cm; \bullet , $x_1=128.4$ cm; \blacktriangle , $x_1=189.4$ cm).

$$\int_{-\infty}^{\infty} \epsilon dx_2 = \nu \int_{-\infty}^{\infty} \omega^2 dx_2, \quad (4)$$

where $\omega^2 = \overline{\omega_i \omega_i}$ is the enstrophy. We thus have

$$\frac{\mathcal{E}}{\Delta U^3} = \nu \int_{-\infty}^{\infty} \frac{\omega^2}{\Delta U^3} dx_2 = \int_{-\infty}^{\infty} \frac{\nu \delta_m \omega^2}{\Delta U^3} d\xi, \quad (5)$$

where $\xi = x_2/\delta_m$. Since $\mathcal{E}/\Delta U^3$ is constant during self-similarity, the integrand of the nondimensionalized integral on the right of (5) should collapse when plotted against ξ . Thus the correct self-similar scaling for the enstrophy, and by extension all components of the vorticity tensor $\overline{\omega_i \omega_j}$, is $\Delta U^3/(\nu \delta_m) = \text{Re}_m \Delta U^2/\delta_m^2$. The factor of Reynolds number appears in the scaling because the vorticity statistics are not large-scale quantities. The dissipation *does* scale like a large-scale quantity (no Reynolds number factor) because the dissipation rate is set by the large scales, although the dissipation actually occurs at small scales. When the Reynolds number factor is omitted in the scaling of $\overline{\omega_i \omega_j}$, the profiles increase in magnitude as the flow develops since the Reynolds number is increasing (see Refs. 34 and 35).

Profiles of $\bar{u}_1^2/\Delta U^2$ and $\nu \delta_m \bar{\omega}_3^2/\Delta U^3$ at five different times in the self-similar period are plotted against ξ in Fig. 3. The collapse of the other components of the Reynolds stress and vorticity tensors is equally good.

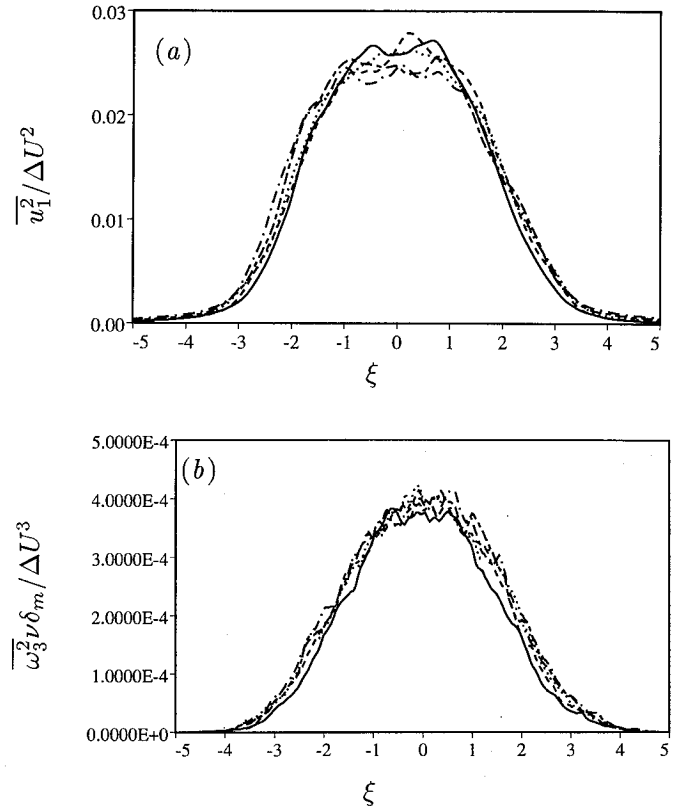


FIG. 3. Collapse of $\bar{u}_1^2/\Delta U^2$ and $\bar{\omega}_3^2 \nu \delta_m/\Delta U^3$ in scaled coordinates at the same five times shown in Fig. 2(b).

Since the Reynolds stress components are indeed self-similar, the scaled Reynolds stresses can be time-averaged in self-similar coordinates to improve the statistical sample of the average quantities. The averaging interval ($105 < \tau < 150$) corresponds to two eddy-turnover times, Λ/q , where Λ is the u_1 integral scale in the x_1 direction and $q^2 = u_i u_i$. The resulting averaged profiles are shown in Fig. 4, along with experimental data from Ref. 5. The agreement between the simulation and the experiment is quite good. The major difference is that the experiment has more intense vertical velocity (u_2) fluctuations, which extend over a wider range of ξ . There is a similar, but less pronounced, difference in the u_1 fluctuations. Interestingly, the $\bar{u}_2^2/\Delta U^2$ simulation profile at $\tau=187.5$ [after the breakdown of self-similarity, dashed line in Fig. 4(b)] agrees much better with the experiment. At this late time, the \bar{u}_1^2 and \bar{u}_3^2 profiles are too low near the center of the layer, but careful examination of Figs. 4(a) and 4(c) reveals that away from the center of the layer these late-time profiles are also in better agreement with the experiment than the average profiles.

Time-averaged profiles of the components of the vorticity tensor are shown in Fig. 5. The streamwise component $\bar{\omega}_1^2$ is about 25% larger than the cross-stream and spanwise components, which are about equal. These relative magnitudes are consistent with vorticity components in the homogeneous shear flow simulations of Rogers and Moin.³⁶ Balint and Wallace³⁴ measured $\bar{\omega}_1^2$ to be about 75% larger than the other components in their experimen-

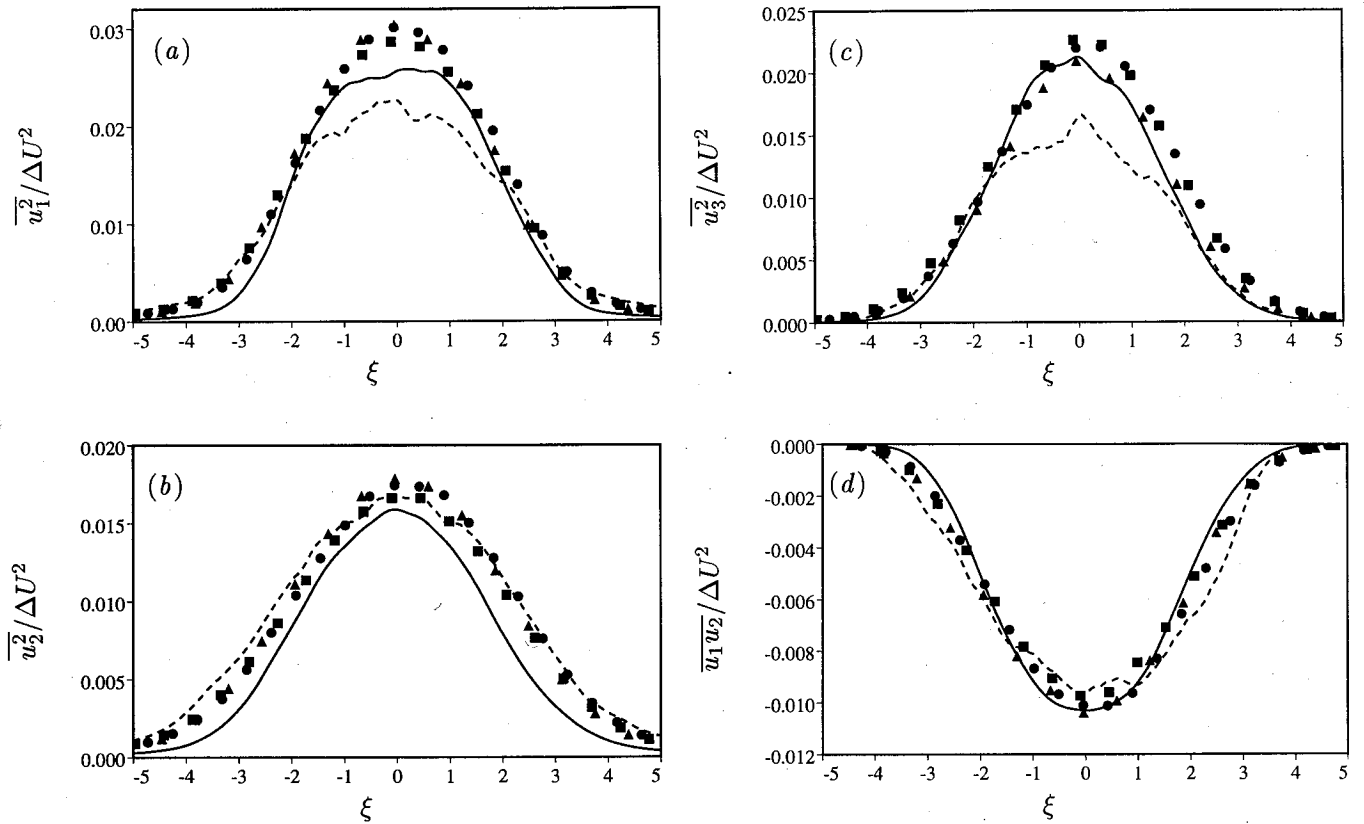


FIG. 4. Comparison of the time-averaged (in scaled coordinates) simulation results for the components of the Reynolds stress tensor (—) with the results of Bell and Mehta (1990) [solid symbols, as in Fig. 2(b)] and the simulation profiles at $\tau=187.5$ (---).

tal mixing layer, but this large ratio is likely the result of inadequate resolution in the measurements.³⁷ The correlation coefficient $\overline{\omega_1 \omega_2} / (\omega'_1 \omega'_2)$ (primes indicating RMS values) is about 0.26 for $|\xi| < 3$ which is a factor of two lower than found in the homogeneous shear simulations of Rogers and Moin. All components of the vorticity tensor are essentially zero for $|\xi| > 4$, unlike the normal components of Reynolds stress, which have slowly decaying tails. This slow decay is due to potential velocity fluctuations. Self-similarity of the small-scale vortical motions, as indicated by the $\overline{\omega_j \nu \delta_m} / \Delta U^3$ profiles, takes slightly longer to achieve than the self-similar collapse of the Reynolds stress

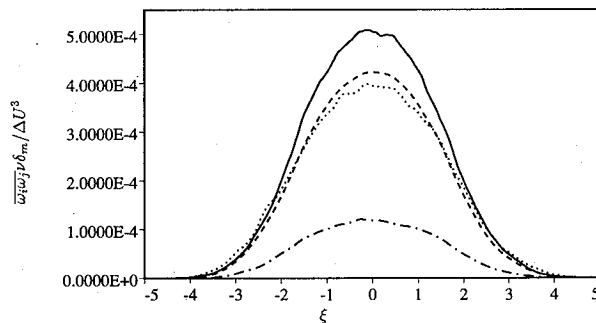


FIG. 5. Comparison of the time-averaged (in scaled coordinates) simulation results for the components of the vorticity tensor $\overline{\omega_j \omega_k}$. —: $\overline{\omega_1 \omega_2 \nu \delta_m} / \Delta U^3$, ---: $\overline{\omega_2^2 \nu \delta_m} / \Delta U^3$, ·····: $\overline{\omega_3^2 \nu \delta_m} / \Delta U^3$, - · - ·: $\overline{\omega_1 \omega_2 \nu \delta_m} / \Delta U^3$.

profiles. However, the collapse of vorticity statistics persists until the end of the simulation, well after $\tau \approx 150$. This suggests that the loss of self-similarity at $\tau \approx 150$ is caused by the evolution of large-scale flow features.

From Fig. 2(a), the dimensionless layer growth rate

$$r = \frac{1}{\Delta U} \frac{d\delta_m}{dt} = \frac{d(\delta_m/\delta_m^0)}{d\tau} \quad (6)$$

can be calculated to be 0.014 during the self-similar period. Note that for spatially developing mixing layers the equivalent quantity is the same as r_ω in (1) with δ_ω replaced by δ_m . The ratio of the vorticity thickness growth rate [r_ω , see (1)] and momentum thickness growth rate is the ratio of the vorticity to momentum thicknesses ($r_\omega = 4.8r$ for this flow). The range for r in “unforced” experiments quoted by Dimotakis³⁸ is from 0.014 to 0.022. [Dimotakis quotes the visual thickness growth rate. We used his suggested factor of two to relate the “visual” thickness to the vorticity thickness, and we used the ratio of vorticity thickness to momentum thickness for an error function mean velocity profile (4.44) to obtain the range quoted here.] The numerical simulation results thus lie at the low end of this growth rate range, however, they agree fairly well with the growth rate of 0.016 obtained by Bell and Mehta.⁵ This agreement might be expected given the good agreement of the Reynolds shear stress shown in Fig. 4(d). The mean momentum equation provides a direct relationship between the centerline value of $-\overline{u_1 u_2} / \Delta U^2$ and the growth rate r

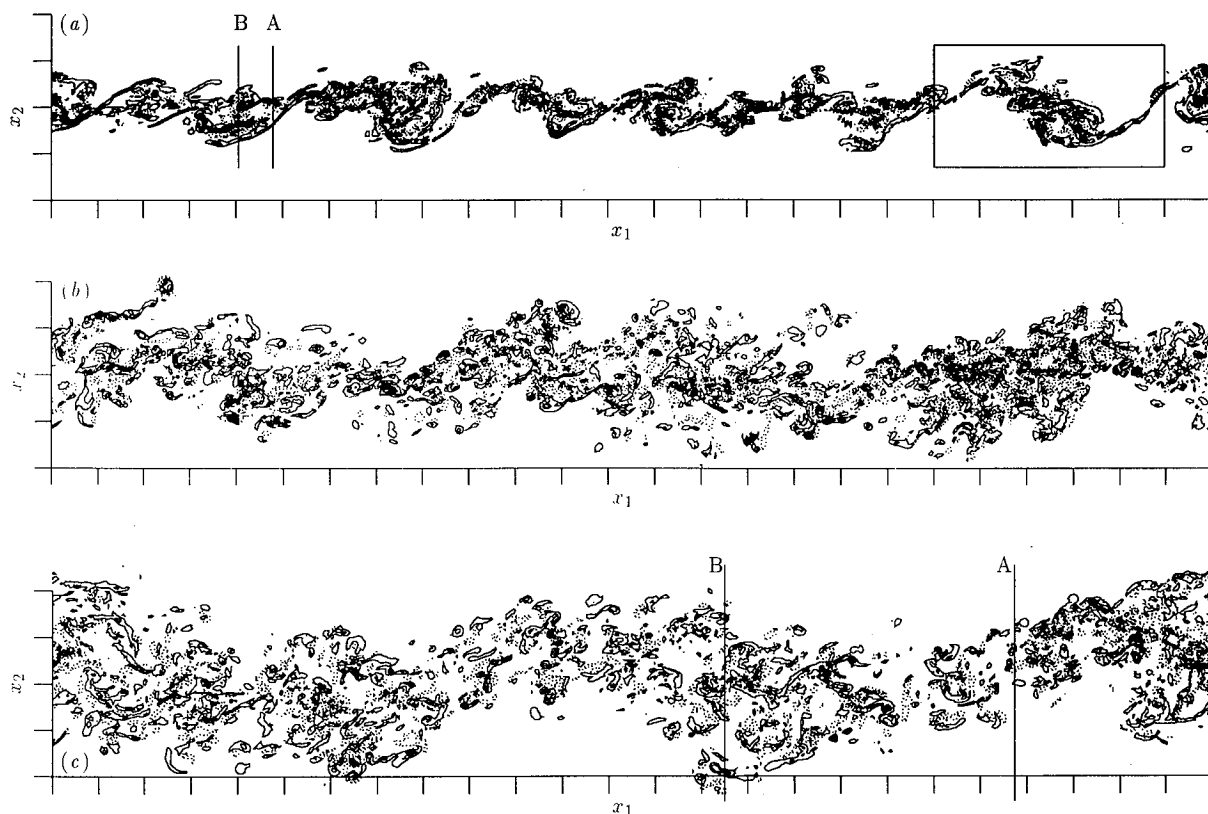


FIG. 6. Contours of spanwise vorticity in x_1 - x_2 planes at (a) $x_3 = 18.8\delta_m^0$ and $\tau = 78.5$, (b) $x_3 = 0$ and $\tau = 150.0$, and (c) $x_3 = 0$ and $\tau = 187.5$. Contour increments are ± 0.25 , positive contours are dotted, and tic marks are at $5\delta_m^0$ increments. The vertical lines mark the locations of the x_3 - x_2 planes depicted in Figs. 10 and 11. The evolution of the region marked by the box in (a) is shown in Fig. 8.

for a given mean velocity profile shape, and the velocity ratio of 0.6 used in Ref. 5 is sufficiently large for the temporally and spatially evolving layers to be similar.

At $\tau = 120$, when the layer is self-similar, the momentum thickness of the mixing layer has only grown by a factor of 2 [see Fig. 2(a)], which is small compared with the growth required to attain self-similarity in many experiments (e.g., a factor of about 10 in Ref. 39, and a factor of about 9 in Ref. 40). There are two likely explanations for this difference. First, the inlet mean velocity profiles are different in the experiments and the computations. The experimental profiles, being asymmetric and containing a wake component, may require more development to become self-similar. Second, the experiments may inadvertently include organized disturbances (e.g., two-dimensional disturbances resulting from the receptivity of the splitter-plate tip). It may take a long time for the effects of these disturbances to be eliminated. It is also possible that the effects of such disturbances would extend into the self-similar regime, as suggested by Dimotakis and Brown.⁹

B. Structure of the baseline mixing layer

The statistical properties presented in Sec. III A suggest that the TBL simulation is indeed self-similar and in fairly good agreement with experimentally measured self-similar turbulent mixing layers. Two differences with the experimental data of Bell and Mehta⁵ are the smaller cross-stream velocity variances and the somewhat lower growth

rate. The mixing layer is well known for its coherent structures (e.g., rollers and rib vortices), and it seems likely that these fairly minor disagreements with the experiment may be manifestations of some difference in the coherent structures. Since the simulation and the experiments have important geometric differences (e.g., the splitter-plate tip), such differences in the large-scale structure are plausible. The structural features of the TBL simulation are discussed below to investigate this issue and to document the structural properties of a particular self-similar turbulent mixing layer.

1. Spanwise rollers and pairing

Contours of spanwise vorticity (ω_z) in x_1 - x_2 planes of the mixing layer (Fig. 6) show that there are clumps of spanwise vorticity (rollers) interspersed with thinner regions that have less spanwise vorticity (braids) both before ($\tau = 78.5$), during ($\tau = 150.0$), and after ($\tau = 187.5$) the period of self-similarity discussed in Sec. III A. At the later two times, braid regions contain many small-scale vorticity fluctuations, as do the rollers. However, at $\tau = 78.5$ there are at least some braid regions that are nearly devoid of spanwise vorticity. These "clean" braids are similar to those found in laminar and transitional mixing layers (e.g., Refs. 19 and 41).

To study the large-scale structures in more detail, a diagnostic that will locate the rollers and braid regions in x_1 and x_3 is needed. This is similar to the situation in experiments, where a structure must be detected so that it

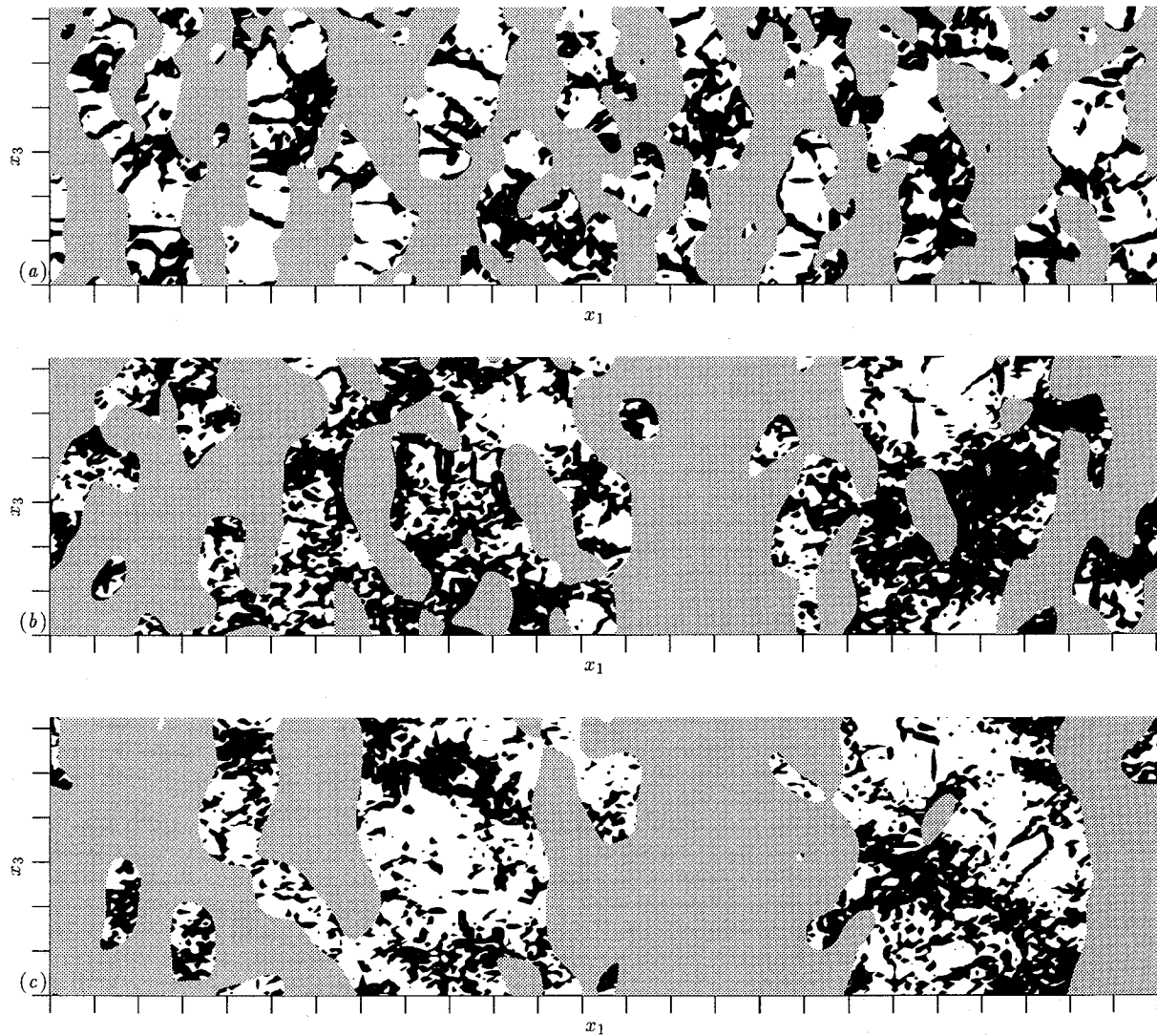


FIG. 7. Locations in x_1 and x_3 of the rollers (gray), as determined by $\mathcal{R} < 0$ at (a) $\tau=78.5$, (b) $\tau=150.0$, and (c) $\tau=187.5$. Also shown (in black) are the locations where the maximum enstrophy exceeds $2.4\Delta U^2/\delta_m^0$. Tic marks are at $5\delta_m^0$ intervals.

can be included in an ensemble average of similar structures. In this case, however, we wish to map the location and size of the structures in space; no averaging is to be done. The results of Rogers and Moser¹⁹ suggest that the most important difference between the braids and rollers is the strain dominance of the former and the rotation dominance of the latter. To this end, we consider the two quantities,

$$\Omega = -\frac{1}{2} \int_{-\infty}^{\infty} \omega_3 dx_2 \quad \text{and} \quad \Sigma_{ij} = \int_{-\infty}^{\infty} S_{ij} dx_2, \quad (7)$$

where S_{ij} is the strain-rate tensor, and the cross-stream integral eliminates some of the contributions of small-scale features. When normalized by the local thickness, these quantities are measures of the large-scale vorticity and strain-rate tensor. The layer may be said to be strain dominated where the principal value of Σ_{ij} in the plane normal to the mean vorticity is greater than Ω . This condition reduces to⁴²

$$\frac{\partial V}{\partial x_1} = \frac{\partial}{\partial x_1} \int_{-\infty}^{\infty} u_2 dx_2 > 0, \quad (8)$$

where this serves as the definition of V . It is expected that $\partial V/\partial x_1$ will be negative where there are rollers and will be positive where there are braids, and indeed this is the case for the flow considered here. However, variations in $\partial V/\partial x_1$ are still dominated by small scales. To extract the large-scale behavior of $\partial V/\partial x_1$, it is filtered in x_1 and x_3 with a Gaussian filter to obtain the roller diagnostic

$$\mathcal{R} = \int_{x'_1} \int_{x'_3} G(x_1 - x'_1, x_3 - x'_3) \frac{\partial V}{\partial x_1} dx_1 dx_3, \quad (9)$$

where G is the bivariate Gaussian filter kernel, with a width chosen to be equal to the momentum thickness δ_m of the mixing layer, and rollers are defined as regions where $\mathcal{R} < 0$.

The \mathcal{R} diagnostic is shown in Fig. 7 at the same times examined above ($\tau=78.5$, 150.0, and 187.5). It suggests

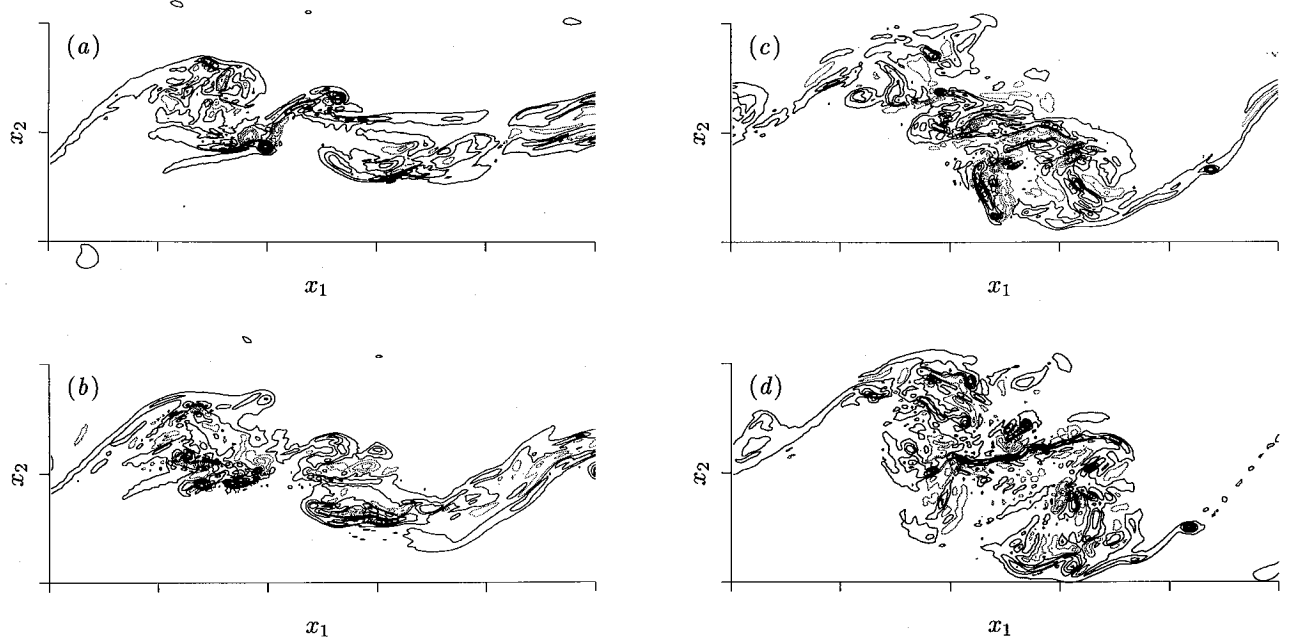


FIG. 8. Contours of spanwise vorticity in the x_1 - x_2 plane at $x_3 = 18.8\delta_m^0$ and (a) $\tau = 59.4$, (b) $\tau = 66.3$, (c) $\tau = 78.5$, and (d) $\tau = 85.9$. The domain depicted is marked with a box in Fig. 6(a). The contour increment is $\pm 0.4\Delta U/\delta_m^0$, positive contours are dotted, and tic marks are at $5\delta_m^0$ intervals.

that there are rollers and braid regions in the flow at all three times, in agreement with the contour plots in Fig. 6. The \mathcal{R} diagnostic also gives an indication of the spanwise coherence of the structures. At $\tau = 78.5$, the structures have a spanwise extent that is larger than the streamwise spacing, but they are not two dimensional. There are about eight rollers in the streamwise domain shown. In contrast, the structure in the center of the x_1 domain at $\tau = 150.0$ does span the domain in x_3 . Toward the edge of the x_1 domain at this time the structures are not as well organized, but they appear to be conglomerating into a second large roller, which is visible on the domain boundary at $\tau = 187.5$. Since the spanwise domain size is smaller than the streamwise spacing of the structures at these late times, it is not possible for the rollers to have the spanwise variations that were present earlier [Fig. 7(a)]. Thus the late-time two-dimensionality of the rollers is an artifact of the computation. It is likely that the constraints imposed by the finite spanwise (and streamwise) domain size and the resulting two-dimensionality of the rollers are responsible for the loss of self-similarity at late time (Sec. III A). Remarkably, the number of structures in the streamwise direction has decreased by a factor of about 4 between the times depicted in Fig. 7, while the momentum thickness has only increased by a factor of 2. This is consistent with the fact that the rollers appear more elongated in the streamwise direction at $\tau = 187.5$ [Fig. 6(c)].

The roller structures in this flow have clearly increased their streamwise length scale, so one wonders if they did so by the "classical pairing" mechanism associated with laminar rolled-up mixing layers, as described by Winant and Browand.⁴³ At the earlier time (before self-similarity), pairing apparently does occur. The two rollers in the box in Fig. 6(a) are rotating about each other, as can be seen in Fig. 8. This pairing only occurs locally in the spanwise

direction, as can be seen in Fig. 9, where the \mathcal{R} diagnostic is shown in the same x_1 domain and at two of the times depicted in Fig. 8. At the earlier time, the two rollers shown have begun to merge locally near the center of the x_3 domain, and later, a single roller remains, which does not span the entire x_3 domain. Such local pairings are similar to those observed in the experiments of Chandrsuda *et al.*¹¹ and in several computations of transitional mixing layers.^{12,13}

However, after self-similarity, no such organized pairings have been detected. When the self-similar structures change scale, the vorticity from one roller appears to ooze gradually into its neighbors, without the corotation characteristic of pairing. It is instructive to note here that although Brown and Roshko⁸ did observe a scale increase of their large-scale structures as the flow evolved, they did not observe classical pairings in their turbulent layers ($Re_m \approx 14\,000$). Also, Hussain and Zaman³⁹ were unable to detect pairings in their self-similar turbulent mixing layer ($Re_m \approx 85\,000$). It is not surprising that these high-Reynolds number turbulent mixing layers exhibit different behavior than that observed by Winant and Browand,⁴³ because Winant and Browand's experiment was done at very low Reynolds numbers (Re_m of up to 150). As a result, their mixing layer growth rate $r = 0.012$ is low, and the variance of the streamwise velocity fluctuations is only $0.01\Delta U^2$. Their flow visualizations suggest that the flow consists of laminar rollers.

Moore and Saffman⁴⁴ proposed an alternative amalgamation mechanism that seems to better describe the process taking place in the simulations. They examine a model problem consisting of an array of two-dimensional elliptical vortices of uniform vorticity [with major axes horizontal as suggested by Fig. 6(c)] and conclude that if the centers of the vortices are within $3.5\delta_\omega$ of each other, a

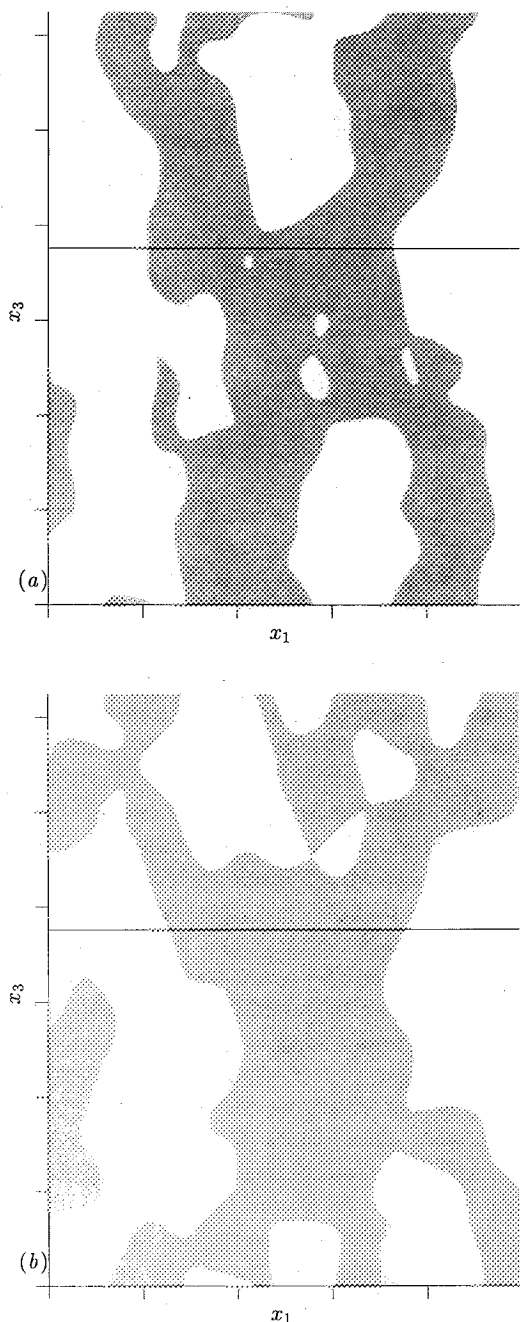


FIG. 9. Locations in x_1 and x_3 of the rollers (gray), as determined by $\mathcal{R} < 0$ at (a) $\tau=66.3$ and (b) $\tau=85.9$. The x_1 domain depicted is that shown in Fig. 8 and marked by the box in Fig. 6. The black horizontal line marks the x_3 location of the plane shown in Fig. 8. Tic marks are at $58m$ intervals.

vortex will be torn apart by the strain field of its neighbors. They expect mixing layer vortex cores to continually grow by turbulent diffusion, eventually becoming large enough so that some vortices are torn apart, with their vorticity being absorbed (perhaps unequally) between their neighbors. Dimotakis and Brown⁹ observed this “tearing” process in a mixing layer experiment at $Re_\omega \approx 130\,000$. At the end of the numerical simulation, the vorticity thickness is about $13.6\delta_m^0$, and therefore the Moore and Saffman criterion would require about $47\delta_m^0$ between eddies; this would permit at most 2.6 eddies in the computational domain.

This is in good agreement with the fact that the number of “rollers” appears to have been recently reduced to 2 at the end of the simulation (Fig. 7).

2. Rib vortices

In laminar and transitional mixing layers, the dynamics of the braid region and those of the roller are different due to the strain dominance of the former and the rotation dominance of the latter.¹⁹ In particular, the braid region is apparently susceptible to a three-dimensional instability, resulting in the formation of streamwise rib vortices. We will thus examine the simulated flow at the three times examined in Sec. III B 1 ($\tau=78.5$, 150.0, and 187.5) for evidence of rib vortices.

Shown in Fig. 7 along with \mathcal{R} are the high-entropy regions in the braids. At $\tau=78.5$, the ribs are visible as the long, thin, roughly streamwise vortices spanning many of the braid regions. Direct examination of these vortices shows that they behave very much like their counterparts in pretransitional and transitional flows (e.g., Refs. 19 and 30). At $\tau=150.0$ and 187.5, however, there are no clear rib vortices. There are some small-scale vortices visible in the braid region, but none of them extends across an entire braid region. In addition, there does not appear to be any preference for the small-scale vortices to occur in the braid region. The high-entropy regions in the rollers (not shown) at the two later times are similar to those in the braids, though denser. The small-scale vortices at this time appear to be the “worms” that have been found to be a common feature of turbulent flows by Jimenez.⁴⁵ He suggested that turbulent flows have worm vortices with circulation Reynolds numbers (Γ/ν) between 200 and 400. Estimates of the circulations of the strong vortices in the braid regions at $\tau=187.5$ are of this order. However, estimates of rib-vortex circulations in the flow at $\tau=78.5$ are as much as 800, suggesting that these vortices represent more than just small-scale turbulent structure.

Contours of streamwise vorticity and the passive scalar in the braid regions (x_3-x_2 planes marked by the vertical lines labeled “A” in Fig. 6) and rollers (planes marked “B” in Fig. 6) are shown for the two times $\tau=78.5$ and 187.5 in Figs. 10 and 11. These rollers and braids were selected because they are the most spanwise coherent (see Fig. 7). At $\tau=78.5$, the strong streamwise vorticity in this plane is dominated by compact approximately circular regions of intense vorticity. The passive scalar contours indicate a sharp interface in the scalar, and this interface is rolled up around the streamwise vortices. These features are characteristic of ribs in the braid regions of nonturbulent mixing layers. In contrast, the streamwise vorticity at $\tau=187.5$ (Fig. 11) is not well organized, although there are a few small circular regions of intense vorticity. The scalar at this time does not have the single sharp interface with discrete roll-ups seen at the earlier time. Comparing the braid region [Fig. 11(a)] to the roller core [Fig. 11(b)] suggests that at $\tau=187.5$ the major difference between the braid and roller is that the vortical region in the braid is thinner in the x_2 direction.

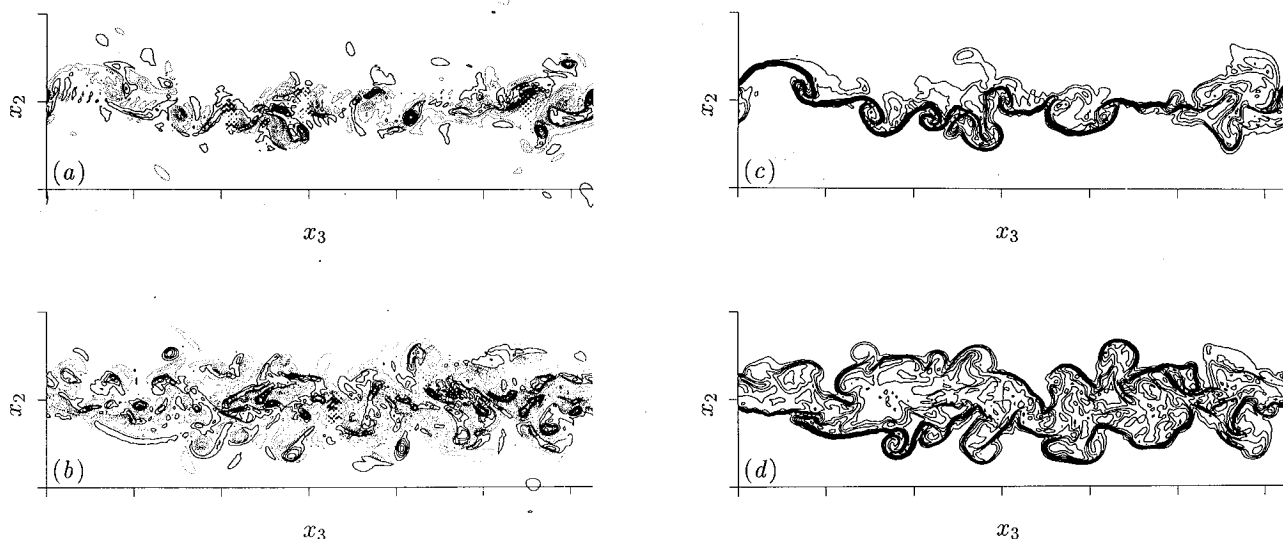


FIG. 10. Contours of (a),(b) streamwise vorticity and (c),(d) passive scalar in the x_3 - x_2 plane at the line marked (a),(c) A (braid region) and (b),(d) B (roller) in Fig. 6(a) at $\tau=78.5$. The contour increment is (a),(b) $0.3\Delta U/\delta_m^0$, (c),(d) 0.1, negative contours are dotted, and tic marks are at $5\delta_m^0$ intervals.

While the structure of the turbulence in the braids and rollers appears to be similar at $\tau=187.5$ (and $\tau=150.0$), the large-scale deformation imposed on the turbulence is different in the two regions. This was implicit in our use of the diagnostic \mathcal{R} , which measures the relative contribution of two-dimensional strain and rotation to the large-scale deformation. The braid regions are strain dominated with strain rates as much as twice the rotation rates, while the rollers are rotation dominated, also by as much as a factor of 2.⁴²

The lack of ribs and pairings in our self-similar flow is different from several experiments (e.g., Refs. 20, 21, and 23), in which flow visualization of turbulent mixing layers suggests that ribs and pairings are present. A possible explanation for this difference is the disturbance environment in the experiments, which may include much stronger two-dimensional or quasi-two-dimensional disturbances than are present in the current simulations. Such disturbances might arise due to the receptivity of the splitter-plate tip.¹⁰ A lack of two-dimensional (or quasi-two-dimensional) disturbances could also account for the lower u_2 variances and lower growth rates of the simulated mixing layer. The effect on u_2 variances is plausible since simulations by Moser and Rogers³⁰ of transitional mixing layers with forced two-dimensional disturbances do yield larger u_2 variances [several times the values shown in Fig. 4(b)]. Also, in the experiments of Bell and Mehta⁵ begun from laminar boundary layers, upstream stations (before self-similarity), where quasi-two-dimensional disturbances are expected to be dominant, have a higher u_2 variance. Simulations with enhanced two-dimensional disturbances were made to investigate this issue; they are discussed in Sec. IV below.

IV. EFFECT OF TWO-DIMENSIONAL FORCING

To investigate the effect of stronger two-dimensional disturbances, two additional simulations, FTBL and GTBL, were made.

The initial conditions for both flows were the turbulent boundary layer conditions used in the TBL simulation described in Sec. III, plus additional two-dimensional disturbances. Adding energy to a two-dimensional mode of a particular frequency, as well as to its subharmonics, would result in a forced mixing layer with a thickness that does not grow linearly in time due to the organized roller mergings that would result. In an effort to preserve the self-similar linear growth found in the TBL simulation and to mimic the lack of phase coherence likely in experimental situations, the energies of the two-dimensional modes in the turbulent initial condition were amplified without changing the relative amplitudes and phases between them. Since the two-dimensional modes that are likely to be introduced by a splitter-plate tip would probably not have a significant u_3 component, and because the modes responsible for the roll-up of the mixing layer have no u_3 component, only the u_1 and u_2 fluctuating two-dimensional velocity components were amplified. In the FTBL initial condition these velocities were amplified by a factor of 5, in GTBL they were amplified by a factor of 20. The average (in x) y -integrated energy per unit mass added to the initial conditions as a result of this forcing was $0.0079\Delta U^2\delta_m^0$ and $0.1784\Delta U^2\delta_m^0$ for FTBL and GTBL, respectively, which amounts to 32% and 91% of the total disturbance energy in these cases.

A. Statistics of the forced layers

The evolution of the momentum thickness in the TBL, FTBL, and GTBL simulations is shown in Fig. 12(a). The additional two-dimensional energy in the initial conditions of the FTBL and GTBL simulations results in more rapid layer growth early in the flow development. The Reynolds-stress profiles in the FTBL simulation indicate that the flow is approximately self-similar over roughly the same time period as the TBL simulation (i.e., from $\tau \approx 100$ until the end of the simulation at $\tau=150.0$). During this self-

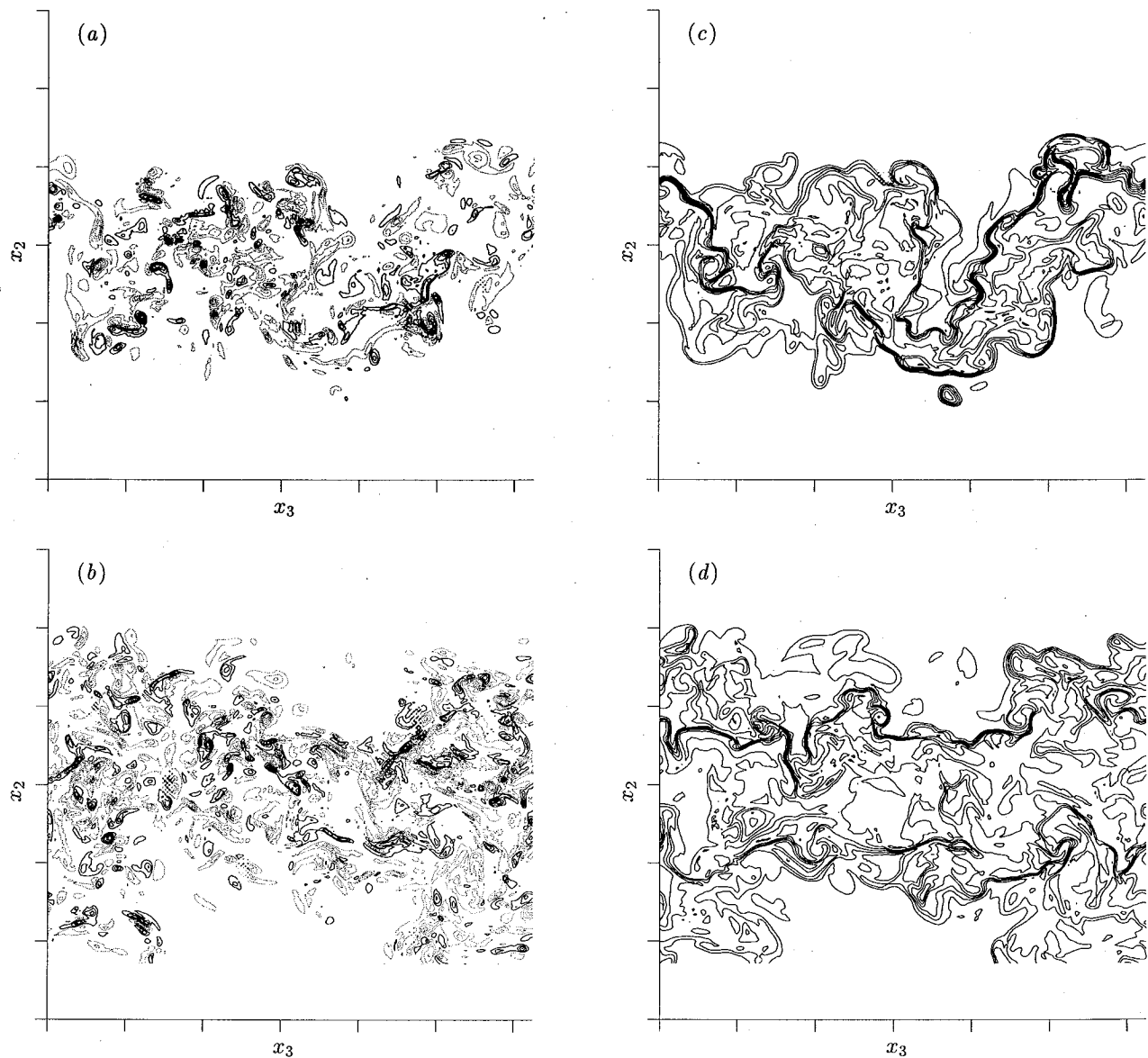


FIG. 11. Contours of (a),(b) streamwise vorticity and (c),(d) passive scalar in the x_3 - x_2 plane at the line marked (a),(c) A (braid region) and (b),(d) B (roller) in Fig. 6(b) at $\tau=187.5$. The contour increment is (a),(b) $0.3\Delta U/\delta_m^0$, (c),(d) 0.1, negative contours are dotted, and tic marks are at $5\delta_m^0$ intervals.

similar period, the layer growth rate r is approximately the same as in the TBL case (after a period of reduced growth rate for FTBL, the curves are approximately parallel). In FTBL, $\mathcal{E}/\Delta U^3$ [Fig. 12(b)] reaches a maximum at $\tau=113.3$ and decreases about 8% after that. This is not as convincingly constant as in TBL; however, the scaled Reynolds stress and vorticity profiles still collapse about as well as they do in the TBL flow.

The Reynolds-stress profiles in the GTBL simulation, particularly the $\overline{u_1^2}/\Delta U^2$ profile, do not collapse as well as those in the TBL and FTBL simulations. Nevertheless, the collapse is good enough to justify the use of time-averaged profiles (here averaged from $\tau \approx 80$ to $\tau \approx 125$) to determine the impact of such strong initial disturbances on the flow statistics. Although there are distinct oscillations in the evolution of the momentum thickness for the GTBL case [Fig. 12(a)], the average growth rate in the developed

state (roughly between $\tau \approx 50$ and $\tau \approx 125$) is $r=0.017$, or about 20% larger than that in the TBL simulation. The stronger time variation of $\mathcal{E}/\Delta U^3$ for the GTBL case also reflects the lack of true self-similarity in that flow. As expected, the collapse of the vorticity statistics is also somewhat poorer than in the other two cases.

Time-averaged mean-velocity profiles from the TBL, FTBL, and GTBL simulations are shown in Fig. 13. The FTBL profile is similar to that of TBL, although it is not quite as linear over the central portion of the layer. The differences between the GTBL mean profile and those of the other two cases are more noticeable, with a lack of symmetry around $\xi=0$ and a mean gradient that persists for $\xi < -4$.

The time-averaged (in scaled coordinates) profiles of all nonzero components of the Reynolds stress tensor for the TBL, FTBL, and GTBL simulations are shown in

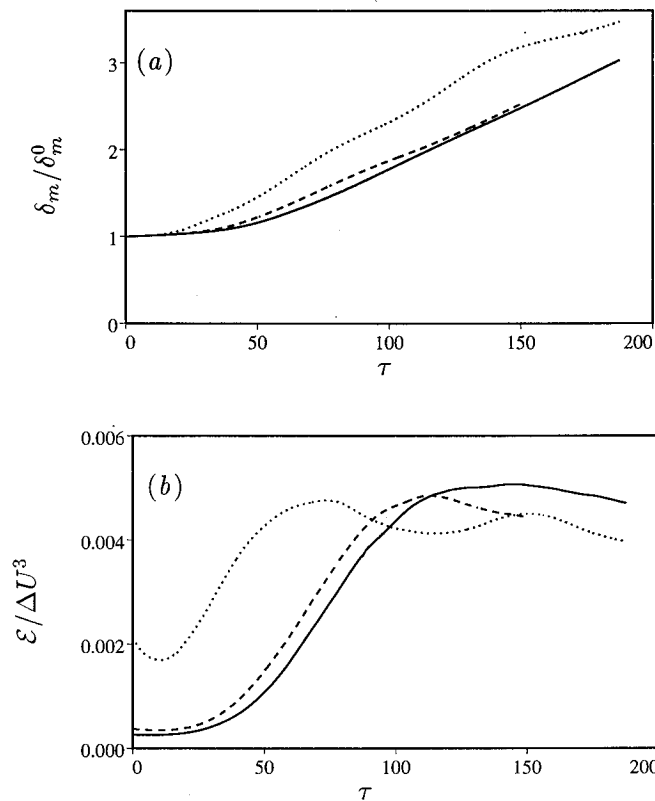


FIG. 12. Time evolution of (a) the momentum thickness δ_m/δ_m^0 and (b) the integrated dissipation $\mathcal{E}/\Delta U^3$ for the —: TBL, ---: FTBL, and ·····: GTBL simulations.

Fig. 14. The trends observed in the profiles for the normal Reynolds stresses with increasing two-dimensional forcing are similar to those observed in the post-self-similar state in the TBL simulation (dashed curves in Fig. 4). The $\overline{u_3^2}/\Delta U^2$, and to a lesser extent $\overline{u_1^2}/\Delta U^2$, profiles are reduced in the center of the layer in FTBL and GTBL. These components also have a somewhat wider extent in ξ . The $\overline{u_2^2}/\Delta U^2$ profiles increase both in width and amplitude, with the amplitude increase for the GTBL case being over a factor of 2. The smaller average level of the centerline $-\overline{u_1 u_2}/\Delta U^2$ in the FTBL layer is consistent with the (slightly) lower average growth rate during the self-similar period [the FTBL momentum thickness in Fig. 12(a) decreases towards the TBL curve after $\tau \approx 100$ before being approximately parallel to it]. Similarly, the increased growth rate for the GTBL case is consistent with the larger centerline level of $-\overline{u_1 u_2}/\Delta U^2$ for that flow. For all Reynolds stress components, an increasing lack of symmetry around the centerline is observed as the two-dimensional mode amplitude is increased. This is a result of the selective amplification of modes in the particular boundary layer realizations used to initialize the simulations.

It should be noted that the results of the Bell and Mehta⁵ experiment are perhaps in better agreement with the FTBL case than with the TBL simulation. The experimental mean velocity data lie in between the results for TBL and FTBL, although they are generally closer to the TBL profile, particularly at the edges of the layer. More striking is that the experimental $\overline{u_2^2}/\Delta U^2$ profile agrees very

well with the FTBL data, whereas the TBL data fall below the experiment (in fact, the experimental data are even slightly above the FTBL results). The widths of the remaining Reynolds stress profiles in the FTBL simulation are also in somewhat better agreement with the experiment. However, the levels of $\overline{u_1^2}$ and $\overline{u_3^2}$ in the center of the layer are lower than those of TBL, and therefore further removed from the experimental values. The good agreement in the level of $\overline{u_2^2}/\Delta U^2$ between the FTBL simulation and the experiments of Bell and Mehta is consistent with the presence of unintended two-dimensional forcing in the experiments, but the discrepancies in the other quantities make this far from certain.

The scaled vorticity tensor component profiles for the FTBL simulation are similar to those shown in Fig. 5 for the TBL flow, although the profiles are slightly wider in ξ and the peak levels of $\overline{\omega_2^2} \nu \delta_m / \Delta U^3$ and $\overline{\omega_3^2} \nu \delta_m / \Delta U^3$ are about 10% lower (this may be due in part to the reduced x_1 resolution of the FTBL simulation in comparison with that used in the TBL case—such reduced resolution will necessarily impact small-scale quantities like vorticity more strongly than large-scale statistics). The differences between the vorticity statistics in the GTBL and TBL simulations are more significant, as might be expected given the large differences in the Reynolds stress profiles. The vorticity tensor component profiles are even wider in ξ than those of FTBL, are asymmetric (peaking near $\xi \approx 0.8$), and have peak levels of only about 70% the peak levels in the TBL simulation.

B. Structure of the forced layers

In addition to the statistical differences between the TBL, FTBL, and GTBL flows noted above, there are notable structural differences. In Fig. 15, the spanwise vorticity in x_1 - x_2 planes is shown for both FTBL and GTBL. The times are during self-similarity for FTBL ($\tau = 150.0$), and approximate self-similarity for GTBL ($\tau = 101.5$). The FTBL vorticity distribution is qualitatively similar to that in TBL at a comparable time [Fig. 6(b)]. The rollers are perhaps slightly more distinct. In GTBL however, the rollers are quite distinct and the braid regions are well formed

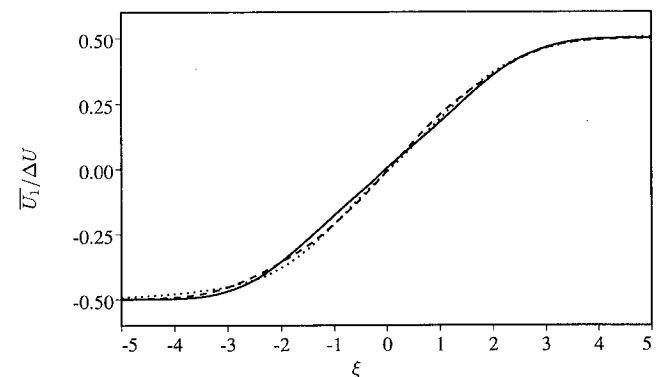


FIG. 13. Comparison of the time-averaged (in scaled coordinates) mean velocity profiles for the —: TBL, ---: FTBL, and ·····: GTBL simulations.

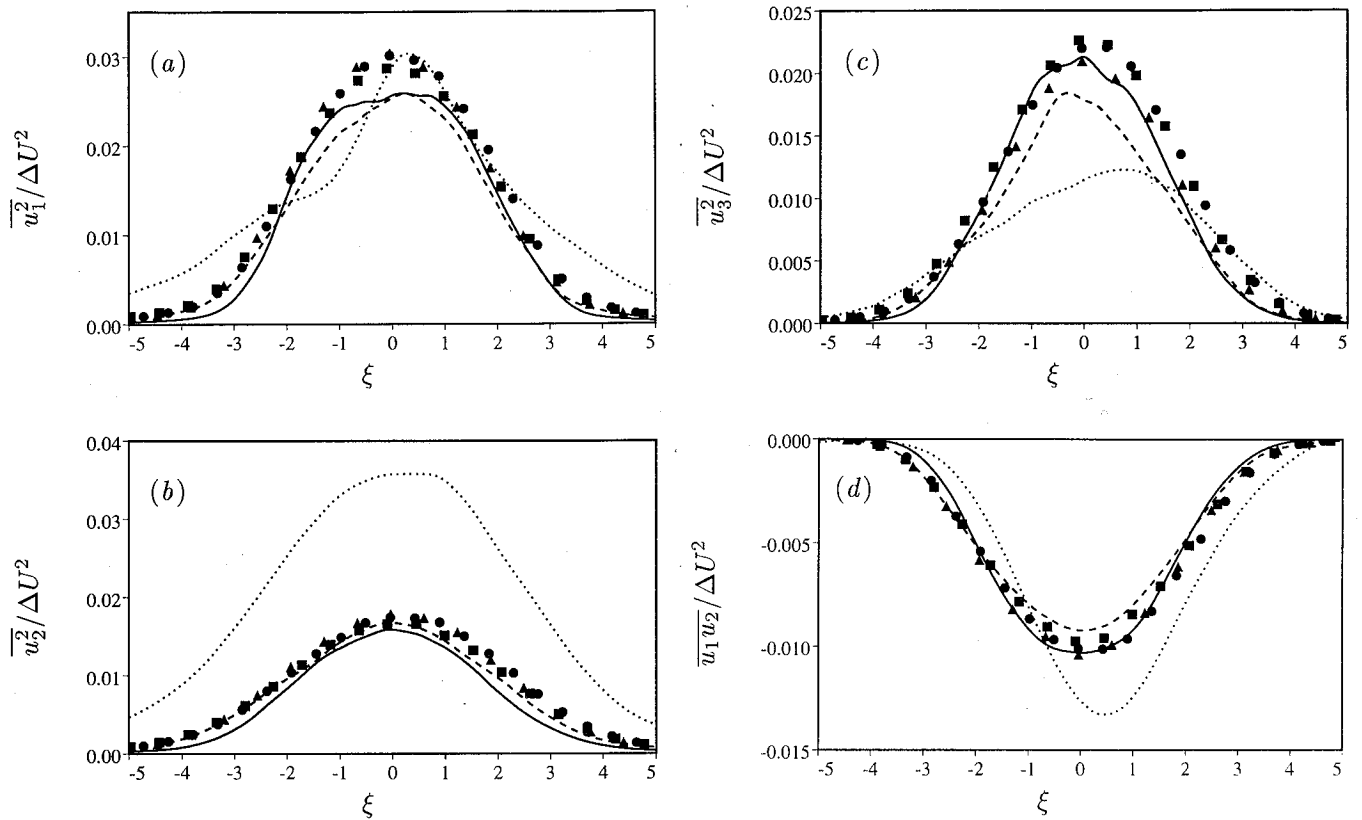


FIG. 14. Comparison of the time-averaged (in scaled coordinates) simulation results for the components of the Reynolds stress tensor for the —: TBL, ----: FTBL, and ·····: GTBL simulations with the experimental data (symbols) of Bell and Mehta (1990) at the same three downstream locations described in Fig. 2(b).

and largely devoid of spanwise vorticity. Furthermore, there is a classical pairing in progress at $x_1 \approx 75\delta_m^0$ (just to the right of the center of the figure). By this time in TBL and FTBL, pairing had ceased and rollers were amalgamating by oozing into each other.

Top views of the roller diagnostic \mathcal{R} and the high-entropy regions are shown in Figs. 16 and 17 for FTBL

and GTBL, respectively. In each case, two times are shown, one before the onset of self-similarity and the other during self-similarity (or approximate self-similarity in the case of GTBL). At the early time, both FTBL and GTBL are similar to TBL [Fig. 7(a)] in that coherent rollers are clearly visible along with apparent rib vortices in the braid region. However, the FTBL and GTBL rollers (as visual-

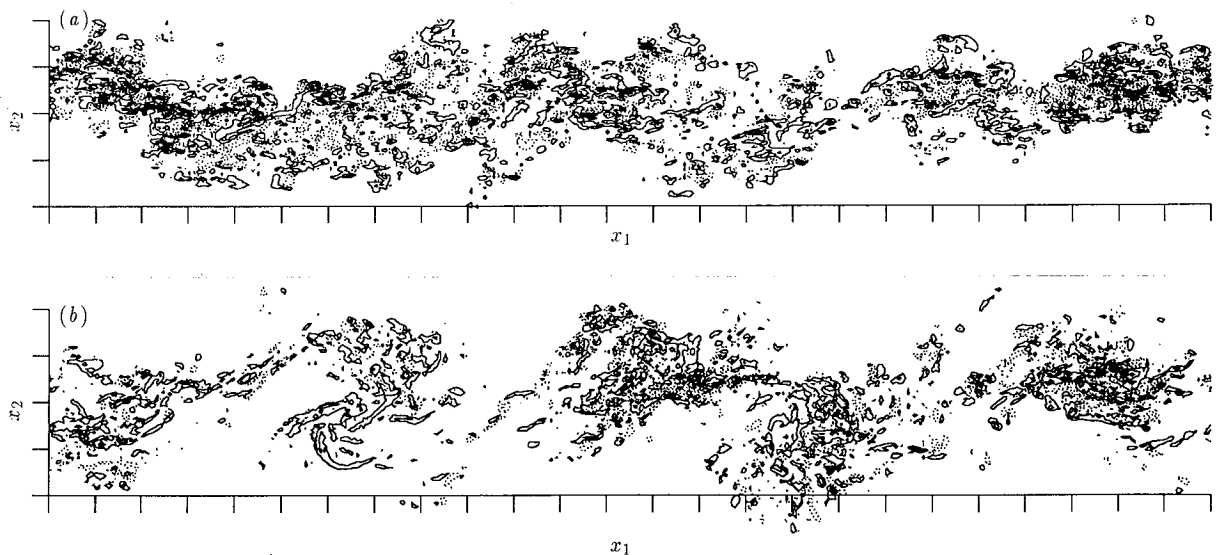


FIG. 15. Contours of spanwise vorticity in x_1 - x_2 planes at (a) $\tau = 150.0$ of FTBL and (b) $\tau = 101.5$ of GTBL. Contour increments are $\pm 0.25\Delta U/\delta_m^0$, positive contours are dotted, and tic marks are at $5\delta_m^0$ increments.

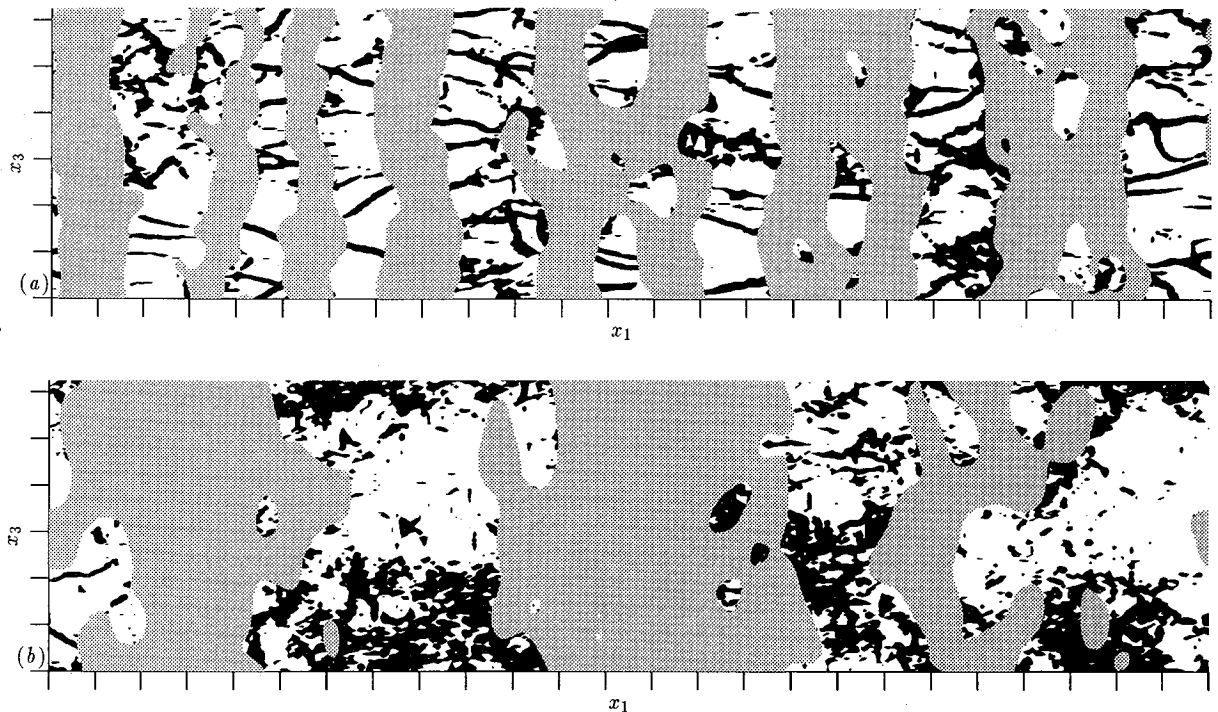


FIG. 16. Locations in x_1 and x_3 of the rollers (gray) in FTBL, as determined by $\mathcal{R} < 0$ at (a) $\tau = 66.8$ and (b) $\tau = 150.0$. Also shown (in black) are the locations where the maximum entrophy exceeds $2.4\Delta U^2/\delta_m^2$. Tic marks are at 58_m^0 intervals.

ized by \mathcal{R}) are more two dimensional than those in TBL, with those in the GTBL case being almost exactly two dimensional. Note that increased roller two-dimensionality has also been observed in simulations of *transitional* mixing

layers in which strong two-dimensional forcing is used.^{12,46} In both FTBL and GTBL, instances of two rollers coming together to amalgamate over the entire spanwise domain are also visible. At later times, FTBL is again similar to

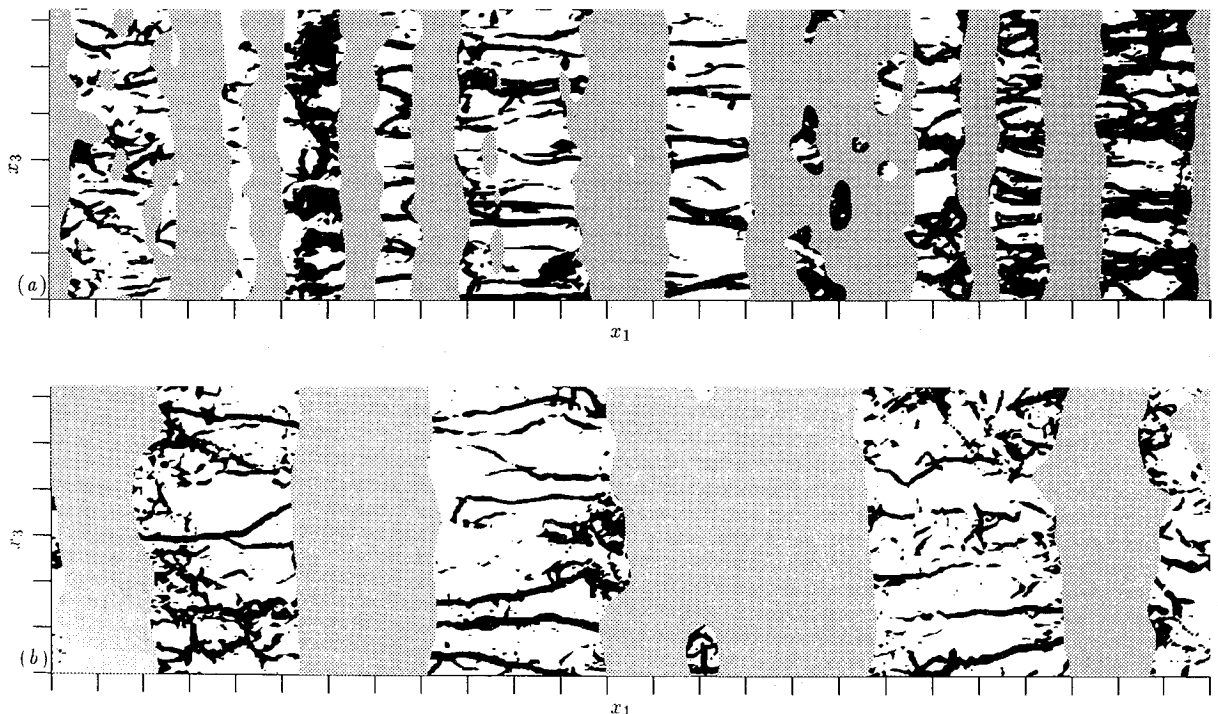


FIG. 17. Locations in x_1 and x_3 of the rollers (gray) in GTBL, as determined by $\mathcal{R} < 0$ at (a) $\tau = 42.1$ and (b) $\tau = 101.5$. Also shown (in black) are the locations where the maximum entrophy exceeds $2.4\Delta U^2/\delta_m^2$. Tic marks are at 58_m^0 intervals.

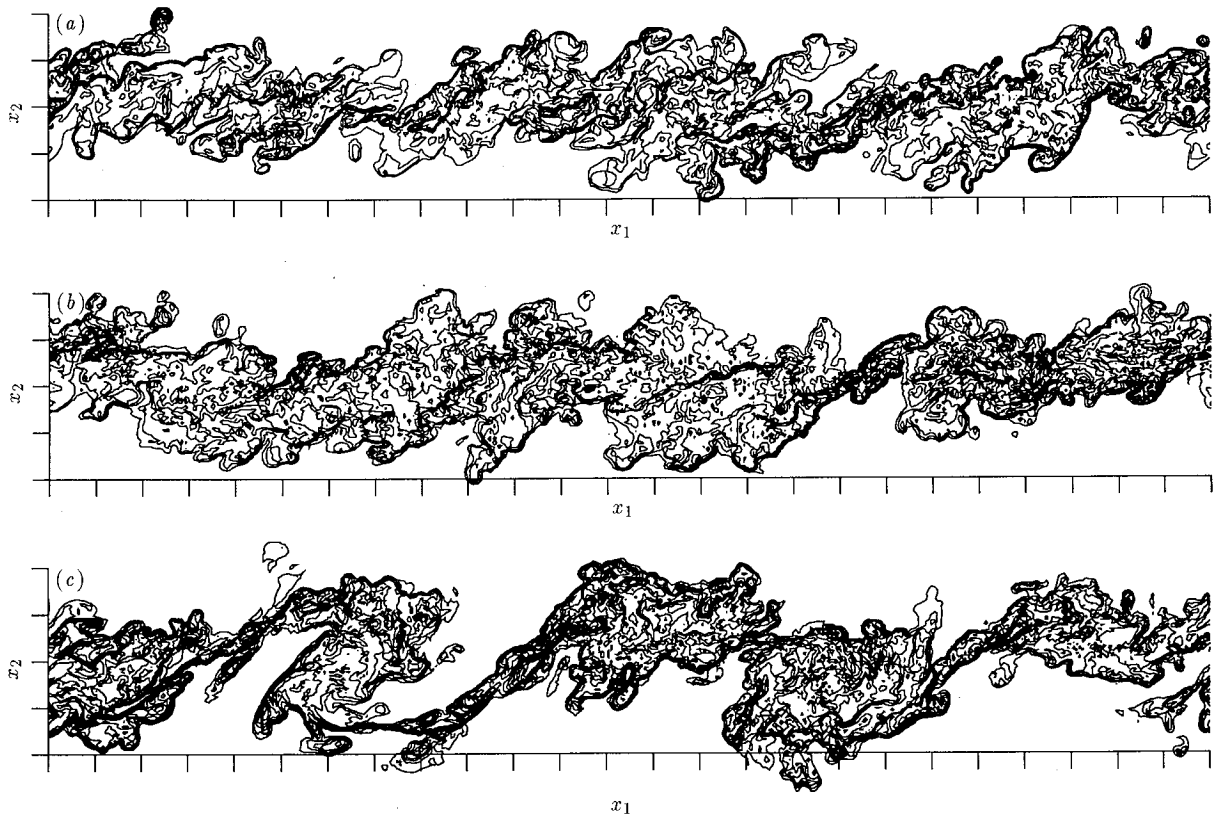


FIG. 18. Contours of the passive scalar in x_1 - x_2 planes for the (a) TBL ($\tau=150.0$), (b) FTBL ($\tau=150.0$), and (c) GTBL ($\tau=101.5$) simulations. Contour increment is 0.1 and tic marks are at $58\delta_m^0$ increments.

TBL in that rib vortices are no longer visible in the braid regions. However, GTBL still has rib vortices even at the late time shown in Fig. 17(b). These results, taken with those of Sec. III B 2, indicate that coherent rib vortices can not survive unless there are well-formed braid regions. Thus, unlike the TBL simulation, GTBL has all the structural features associated with transitional mixing layers (rollers, pairings, and ribs), even at late time.

V. MIXING OF A PASSIVE SCALAR

In each of the cases described in this paper, a passive scalar quantity was simulated in addition to the hydrodynamic fields. The differences in the structure of the mixing layers described above have a significant impact on the mixing characteristics of this scalar.

In Fig. 18, passive scalar contours in x_1 - x_2 planes (side views of the layer) are shown for the TBL, FTBL, and GTBL simulations. The scalar contours illustrate the same structural differences that were outlined above in Sec. IV B. The TBL simulation does not contain “clean” braid regions and shows no evidence of any “classical” pairings. The GTBL simulation, on the other hand, contains both of these features. At the time shown in Fig. 18(c), a pairing is nearing completion (second “roller” from the left) and another is underway (the next two rollers to the right). The FTBL simulation is largely similar to the TBL flow. The pairings in the GTBL flow result in large incursions of irrotational free-stream fluid that penetrate nearly completely across the layer, a feature that is absent in the other

two simulations. This behavior has often been noted in experiments (e.g., Refs. 8 and 23) and has been incorporated into models of the mixing layer.⁴⁷

The structural differences in the passive scalar between TBL, FTBL, and GTBL (Fig. 18) suggest that the mechanism by which free-stream fluid gets mixed into the layer is different in these flows. In GTBL, the free-stream fluid is engulfed into the layer, after which it gets mixed throughout the layer. In contrast, in TBL at late time, fresh fluid is mixed in at the edges of the layer by small-scale eddies. These structural differences result in differences in the character of the scalar PDFs.

The scalar PDFs at several locations with $\xi > 0$ for both early and late times in the TBL, FTBL, and GTBL simulations are shown in Fig. 19, along with results for the WHIGH2P and TURB2P flows described in Ref. 30. The PDFs from the other side of the layer ($\xi < 0$) are statistically symmetric to those shown. Both marching and nonmarching PDFs are found to occur in the simulations. The TBL flow exhibits substantially nonmarching PDFs prior to self-similarity [Fig. 19(a)], but changes to marching PDFs once self-similar [Fig. 19(b)]. The FTBL flow is similar, although it is more convincingly nonmarching prior to self-similarity. The GTBL simulation, on the other hand, is convincingly nonmarching throughout its entire evolution. In fact, it even exhibits a slight “reverse-marching” character, with the most probable scalar value at $\xi \approx 1.0$ being slightly closer to the free-stream value at $\xi = -\infty$ than to that at $\xi = +\infty$.

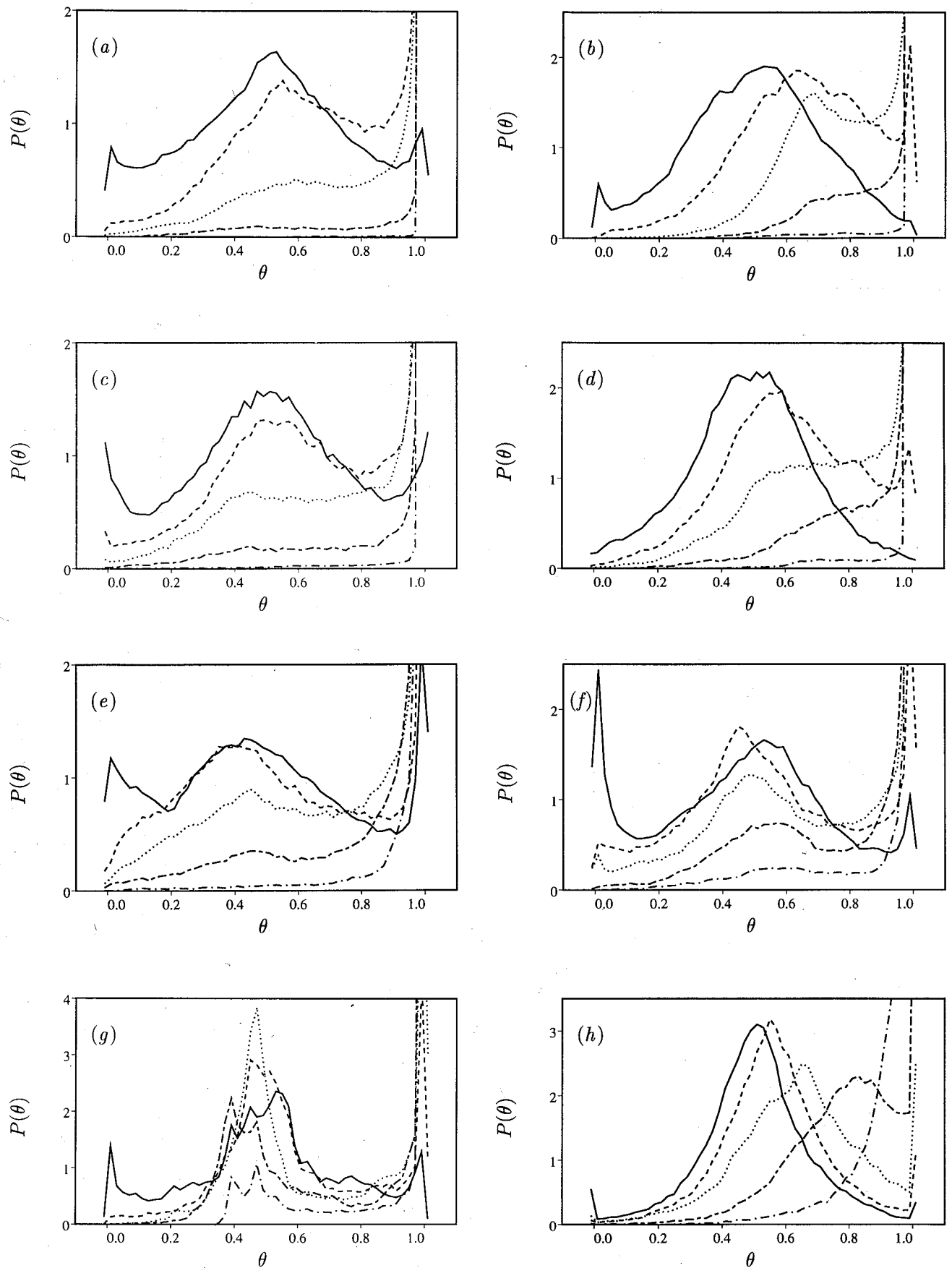


FIG. 19. PDFs of the passive scalar at equally spaced x_2 locations across the layer for (a) TBL at $\tau=85.9$, (b) TBL at $\tau=150.0$, (c) FTBL at $\tau=87.8$, (d) FTBL at $\tau=150.0$, (e) GTBL at $\tau=79.4$, (f) GTBL at $\tau=119.6$, (g) WHIGH2P at $\tau=354.7$ (just after the second pairing), (h) TURB2P at $\tau=423.2$ (just after the second pairing). In frames (a) through (f), —: $\xi \approx 0$, ---: $\xi \approx 1$,: $\xi \approx 2$, - · - ·: $\xi \approx 3$, - - -: $\xi \approx 4$. In frames (g) and (h), the ξ locations are approximately 0.0, 0.9, 1.8, 2.7, and 3.6 (line types in the same order as above).

Thus, as expected, mixing layers that have distinct rollers with clean braid regions and that undergo classical pairings exhibit nonmarching PDFs (GTBL and early time TBL and FTBL). However, the self-similar state achieved by TBL and FTBL does not have these features and therefore exhibits marching PDFs. Further evidence of this is provided by the scalar PDFs from two flows (WHIGH2P and TURB2P) that both undergo a natural transition to turbulence.³⁰ In WHIGH2P, the second pairing is classical, as in GTBL, and the scalar PDFs at that time are nonmarching [Fig. 19(g)]. In contrast, the second pairing in TURB2P is a more gradual amalgamation of the rollers, and it exhibits marching PDFs [Fig. 19(h)].

The scalar PDFs for the WHIGH2P and TURB2P flows are qualitatively different from those of the simulations begun from turbulent boundary layers, in that the levels of the peaks associated with the mixed fluid are significantly higher. In these flows the probability of finding mixed fluid with $\theta \approx 0.5$ is about twice the corresponding value in the TBL, FTBL, and GTBL flows. Examination of the scalar contours indicates that in these two flows, the scalar field consists predominately of large regions of well-mixed fluid in the rollers, surrounded by free-stream fluid with nearly the free-stream scalar value. There is relatively less fluid with intermediate scalar values.

VI. DISCUSSION AND CONCLUSIONS

The numerical simulations of turbulent mixing layers presented in the previous sections evolve self-similarly (or approximately self-similarly) after an initial period during which the flow transitions from boundary layer turbulence to mixing layer turbulence. The self-similarity of the flows is demonstrated by the evolution of the momentum thickness, the evolution of the total dissipation rate of kinetic energy, the collapse of the mean velocity profiles, and the collapse of the Reynolds stress profiles and the vorticity statistics. It was determined that the correct self-similar scaling for the vorticity variances includes a Reynolds number factor because vorticity is a small-scale quantity (see Sec. III A). The values of statistical quantities computed from the simulations are within the range of experimental observations.

The simulation results and much experimental data suggest that the "self-similar state" of a turbulent mixing layer may not be unique.⁹ Different self-similar states may be characterized by different growth rates r , different levels of $u_2^2/\Delta U^2$, different structural features, and different scalar mixing characteristics. We include the GTBL simulation in this discussion despite the fact that the flow is not quite self-similar. It is likely that this lack of self-similarity is an artifact of the time-evolving simulation in a finite spatial domain. In the GTBL flow, the approximate self-similar period is dominated by a few, approximately two-dimensional rollers. Linear growth and self-similarity in experiments are obtained by averaging statistics from the passage of many rollers, which are at varying stages in their evolution. Thus it is reasonable to expect that the GTBL simulation, if performed in a much larger stream-

wise and spanwise spatial domain, would be self-similar. It is quite possible that the reason self-similarity was obtained in the TBL and FTBL computations was because there was relatively little organized large-scale motion in these cases, resulting in a large sample of typical (smaller) eddies in the computational domain.

In the current simulations, the most obvious differences between the alternate "self-similar states" are structural. For example, the difference between Figs. 6(b) and 15(b) is obvious. However, the growth rates of the two flows ($r=0.014$ for TBL and $r=0.017$ for GTBL) are not that different. Both are in the range of experimental observations (0.014 to 0.022).³⁸ It seems likely then, that the experiments referred to by Dimotakis would have structural features ranging from the relative incoherence of TBL (Sec. III B) to organized pairings that are even more prominent than those of GTBL (Sec. IV B).

The reasons for these variations must lie in the disturbance environment. Mixing layers growing from tripped turbulent boundary layers are found to ultimately grow at a slower rate than those originating from laminar boundary layers¹⁰ (except when one of the free-stream velocities is zero). This is also observed in the simulations described here, although the growth rate for cases begun from laminar boundary layers³⁰ is necessarily an average growth rate since the layers are not self-similar. Also, the splitter-plate tip can introduce two-dimensional vortical disturbances into the flow that depend on the downstream environment, including the details of the facility.¹⁰ Thus it is likely that different experiments have substantially different two-dimensional disturbances.

The occurrence of clean braid regions and classical pairings also has a profound effect on the three-dimensional structure of the layer. As suggested by the results of Rogers and Moser,¹⁹ braid regions that are mostly devoid of turbulent fluctuations are necessary for the formation of organized rib vortices. If the braid regions contain substantial turbulent fluctuations, the ribs do not survive (see Sec. III B 2), and the turbulence in the braid regions appears to be no different from that in the rollers.

There is evidence that at least some high-Reynolds-number experimental mixing layers exhibit structural characteristics similar to those of the TBL and FTBL simulations. (Strictly speaking, it is probably the "pairing number" of the flow that is most important in determining the level of flow development rather than the Reynolds number.^{28,48,49}) Jimenez, Cogollos, and Bernal⁵⁰ used a digital image processing technique to generate three-dimensional images from motion pictures taken by Bernal.⁵¹ At $Re_\omega=2400$, they observe pairings of "classical Brown-Roshko eddies," organized streamwise structures, and significant amounts of unmixed fluid inside the layer. Their pictures of a layer at $Re_\omega=10\,000$ are quite different, however. Although some streamwise structure is still apparent, the organization into spanwise rollers is much less pronounced (the layer is of roughly uniform thickness) and no examples of pairing are presented. Also no pockets of unmixed fluid are observed inside the layer; the authors conclude "small-scale turbulence is either produced or

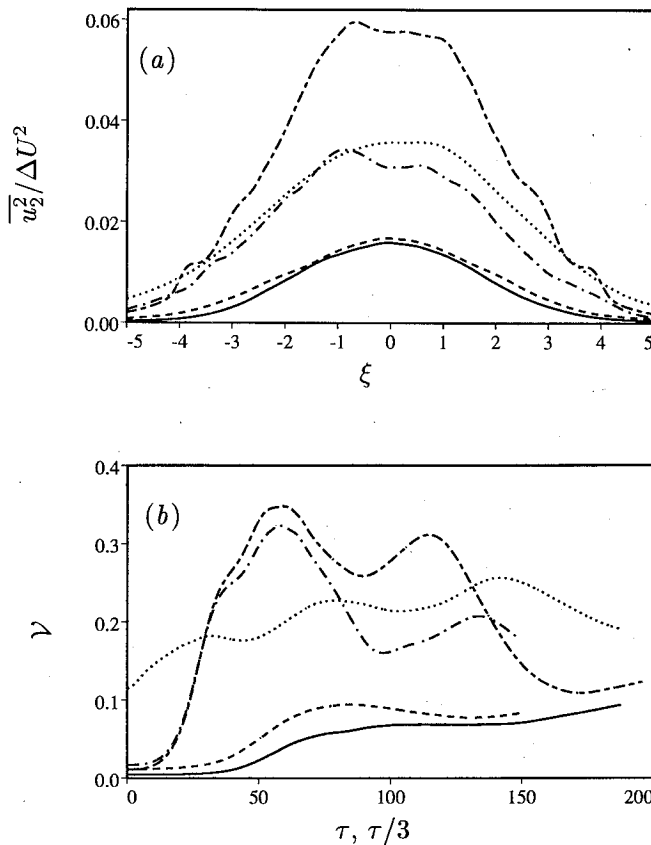


FIG. 20. (a) Comparison of $\overline{u_2^2}/\Delta U^2$ profiles from various simulations, —: TBL time average, ---: FTBL time average,: GTBL time average, - · - ·: WHIGH2P $\tau=354.7$, just after second pairing, - - -: TURB2P $\tau=446.2$, just after second pairing. (b) Time evolution of γ for the same simulations. Note that the WHIGH2P and TURB2P simulations are plotted against $\tau/3$.

convected throughout the layer and mixing is more uniform." They also note that the lack of freshly entrained fluid inside the layer makes it difficult to draw conclusions about the present, as opposed to past, vortex structure. Batt,⁴ in his experiments at Re_ω up to 120 000 noted that the "shear layer is characterized more by random and/or three-dimensional effects than by large-scale two-dimensional coherent structures." The experiments of Brown and Roshko,⁸ although exhibiting coherent structures even in the turbulent state, do show some changes as the Reynolds number increases. In particular, the braid regions between structures become more "filled" with turbulent small-scale eddies and less free-stream fluid is able to penetrate towards the centerline. The experiments of Dimotakis and Brown⁹ attained vorticity thickness Reynolds numbers of about 150 000. Although they did report some pairings, they concluded that "tearing" of an eddy by the strain field of its neighbors, and the resulting absorption of its fluid into the collective motion of its neighboring structures, was also responsible for scale change in their flow, especially at high Reynolds numbers. This tearing mechanism of streamwise scale increase is similar to that observed in TBL and FTBL. Hussain¹⁵ also noted that the "evolution of the large-scale structures in time occurs not through complete pairing, as widely believed, but mostly

through a combination of tearing, fractional pairing between segments torn from different large-scale structures, or partial pairing when one structure captures only a (low-speed) part of a downstream structure."

As discussed in Sec. V, the link between the hydrodynamic structures and the character (marching or non-marching PDFs) of the scalar mixing is clear. Nonmarching PDFs are expected whenever organized rollers with clean braid regions and "classical" pairings dominate the layer. These are necessary to "rapidly" distribute free-stream fluid throughout the thickness of the layer. The marching pdf, which one would expect from an eddy-viscosity model, occurs when the flow is not so well organized.

Differences in $\overline{u_2^2}/\Delta U^2$ are not as obviously related to the structural features of the flows. Values can be significantly larger than those shown in Fig. 4(b). This is often associated with developing mixing layers. Bell and Mehta⁵ measured values as high as 0.11 [about seven times the peak value in Fig. 4(b)] at streamwise locations well upstream of the self-similar region ($Re_m \approx 30$) in an experiment begun from laminar splitter-plate boundary layers. The vertical extent of the u_2 fluctuations was also much wider than that found in the self-similar region. Browand and Weidman⁵² took measurements at "the beginning of the region of linear mixing-layer growth" ($Re_m \approx 60$). At this single streamwise station, the peak level of $\overline{u_2^2}/\Delta U^2$ was found to be 0.024, and the vertical extent of u_2 fluctuations was again larger than that in Fig. 4(b). This resulted in $\overline{u_2^2}/\Delta U^2 > \overline{u_1^2}/\Delta U^2$ over the entire profile, and was attributed to the low Reynolds number of the experiment.

The WHIGH2P and TURB2P simulations described in Ref. 30 both undergo a "natural" transition to turbulence from laminar initial conditions with simple low-wave-number disturbances. After the second pairing of the spanwise rollers, the flows appear "turbulent" ($Re_m = 1170$ and 1120, respectively), but $\overline{u_2^2}/\Delta U^2$ peaks at 0.060 and 0.034, respectively [see Fig. 20(a)]. These levels represent roughly fourfold and twofold increases over the corresponding levels in the TBL flow. The $\overline{u_2^2}/\Delta U^2$ profiles are also much wider than those in the TBL flow and, as observed by Browand and Weidman, $\overline{u_2^2}/\Delta U^2 > \overline{u_1^2}/\Delta U^2$ at all cross-stream locations. Despite the substantially increased level of $\overline{u_2^2}/\Delta U^2$ in the TURB2P simulation, the $\overline{u_1^2}/\Delta U^2$ and $\overline{u_3^2}/\Delta U^2$ profiles are not that different from the late-time profiles (dashed lines in Fig. 4) calculated from TBL.

To investigate this further, consider the dimensionless integrated $\overline{u_2^2}$ energy given by

$$\gamma = \frac{1}{\delta_m} \int_{-\infty}^{\infty} \frac{\overline{u_2^2}}{\Delta U^2} dx_2 = \int_{-\infty}^{\infty} \frac{\overline{u_2^2}}{\Delta U^2} d\xi, \quad (10)$$

shown in Fig. 20(b) for the same five simulations. The GTBL, WHIGH2P, and TURB2P flows are seen to have $\gamma \approx 0.2$ or larger (recall that both WHIGH2P and TURB2P undergo organized pairings). This is in contrast to the TBL and FTBL simulations, where this value remains below 0.1. Also note that γ in WHIGH2P ultimately drops to 0.1, similar to FTBL and TBL. This is well

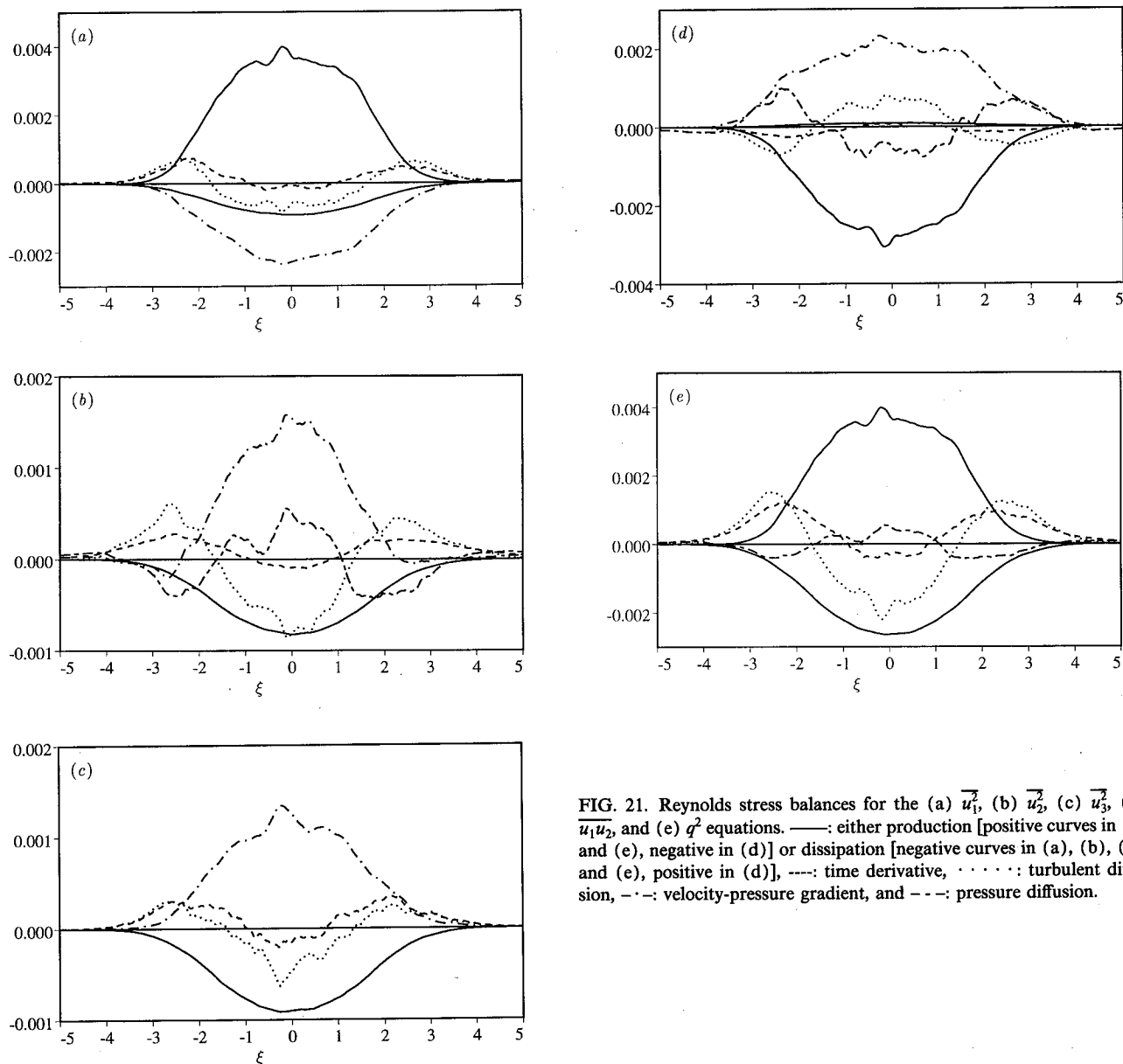


FIG. 21. Reynolds stress balances for the (a) $\overline{u_1^2}$, (b) $\overline{u_2^2}$, (c) $\overline{u_3^2}$, (d) $\overline{u_1 u_2}$, and (e) q^2 equations. —: either production [positive curves in (a) and (e), negative in (d)] or dissipation [negative curves in (a), (b), (c), and (e), positive in (d)], ----: time derivative, ·····: turbulent diffusion, -·-·: velocity-pressure gradient, and ---: pressure diffusion.

after the last pairing in this flow. Thus there does seem to be a link between levels of $\overline{u_2^2}/\Delta U^2$ and ongoing classical pairings. Although pairings do occur at early time in TBL and FTBL, they are infrequent (and not spanwise coherent in TBL) and therefore do not result in a large value of \mathcal{V} . At the second pairing, the level of \mathcal{V} in TURB2P is 65% of that in WHIGH2P. This is apparently related to the difference in the character of the pairings in the two flows. The second pairing in WHIGH2P involves rapid corotation and overturning of the layer. One roller rides up over the top of the other, creating a circular, or even vertically elongated paired roller. The second pairing in TURB2P is delayed relative to that in WHIGH2P. It occurs more slowly, and appears to result from a gradual “oozing” together of the rollers. The final paired eddy is elongated in the streamwise direction (as in TBL), rather than vertically (as in GTBL).

It is likely that differences in roller shape and orientation account for the differences in the level of \mathcal{V} , since an elliptical vortex with a vertical major axis produces more

vertical velocity fluctuations than a vortex with a horizontal major axis.⁵³ When the mixing layer undergoes classical pairings, the rollers tend to be less elongated in the horizontal direction, resulting in higher vertical velocity fluctuations and therefore higher \mathcal{V} . Thus in a self-similar or approximately self-similar mixing layer, the level of \mathcal{V} is an indicator of how dominant clean rollers and classical pairings are. It would be interesting to determine whether experiments exist that exhibit both self-similarity and a high level of \mathcal{V} , and if so, whether flow visualization does indeed indicate the occurrence of classical pairings.

While the simulations suggest that there may be alternate self-similar states, they cannot indicate whether such alternate self-similar states are temporary or will persist indefinitely. In particular, it is not clear whether the organized pairings observed in the GTBL simulation would continue indefinitely if the flow could continue to evolve in a larger computational domain. It is clear, however, that if a universal asymptotic state does exist, it could take a very long time to achieve (see, for example, Ref. 5). This is

consistent with the suggestions of Dimotakis and Brown.⁹ Since the behavior of GTBL is the result of special manipulated initial conditions, we believe that if a universal asymptotic state does exist, it will be like TBL rather than GTBL. This is consistent with recent experiments by Karasso and Mungal²⁸ that indicate that the "ultimate" state of the mixing layer is associated with marching PDFs.

ACKNOWLEDGMENTS

Thanks are due to Rabi Mehta for the raw data from Ref. 5 presented in Figs. 2, 4, and 13. Some of the computations were performed on the NAS supercomputers at NASA-Ames. This paper is dedicated to W. C. Reynolds in honor of his sixtieth birthday.

APPENDIX: REYNOLDS STRESS BALANCES

The governing equation for the evolution of the Reynolds stresses in a time-developing mixing layer can be written as

$$\begin{aligned} \frac{\partial \overline{u_i u_j}}{\partial t} = & - \left(\overline{u_i u_l} \frac{\partial \overline{U_j}}{\partial x_l} + \overline{u_j u_l} \frac{\partial \overline{U_i}}{\partial x_l} \right) - \frac{\partial \overline{u_i u_j u_2}}{\partial x_2} \\ & - \left(\overline{u_j} \frac{\partial \overline{(p/\rho)}}{\partial x_i} + \overline{u_i} \frac{\partial \overline{(p/\rho)}}{\partial x_j} \right) - 2\nu \frac{\partial \overline{u_i} \partial \overline{u_j}}{\partial x_l \partial x_l} \\ & + \nu \frac{\partial^2 \overline{u_i u_j}}{\partial x_2^2}. \end{aligned} \quad (A1)$$

The "time derivative" on the left is thus composed of "production," "turbulent diffusion," "velocity-pressure gradient," "dissipation," and "viscous diffusion" terms, where these terms are given in this order in the above equation (and include minus signs where present). It is also possible to further split the velocity-pressure gradient term into "pressure-strain" and "pressure diffusion" terms,

$$\begin{aligned} & - \left(\overline{u_j} \frac{\partial \overline{(p/\rho)}}{\partial x_i} + \overline{u_i} \frac{\partial \overline{(p/\rho)}}{\partial x_j} \right) \\ & = \frac{p}{\rho} \left(\frac{\partial \overline{u_i}}{\partial x_j} + \frac{\partial \overline{u_j}}{\partial x_i} \right) - \frac{1}{\rho} \left(\delta_{ij} \frac{\partial \overline{p u_j}}{\partial x_2} + \delta_{j2} \frac{\partial \overline{p u_i}}{\partial x_2} \right). \end{aligned} \quad (A2)$$

In these equations, only the mean velocity component $\overline{U_1}$ is nonzero and due to homogeneity, derivatives of averaged quantities with respect to x_1 and x_3 are zero. Thus there is no production term in the $\overline{u_2^2}$ and $\overline{u_3^2}$ equations and no pressure diffusion term in the $\overline{u_1^2}$ and $\overline{u_3^2}$ equations. The equation for $q^2 = \overline{u_i u_i}$ can be obtained by contracting the indices in the above equations. For this equation, the pressure strain is zero and the velocity-pressure gradient term is entirely due to pressure diffusion.

The time-averaged (in scaled coordinates) profiles of each of the balance terms in all the Reynolds stress equations (as well as the q^2 equation) for the TBL simulation are shown in Fig. 21. The viscous diffusion terms are not plotted because they are an order of magnitude smaller than any other term across the entire layer and thus cannot be distinguished from zero in the figure. Note that this is

not the case early in the flow evolution, when the initial boundary layer turbulence has significant viscous diffusion near the "wall," which has just been "removed." The profiles for the FTBL simulation are similar to those for TBL. Those for the GTBL flow show significant differences, including higher levels for the $\overline{u_1^2}/\Delta U^2$, $\overline{u_2^2}/\Delta U^2$, and $\overline{u_1 u_2}/\Delta U^2$ equations, and relatively more turbulent diffusion and less dissipation. They are not presented here because of the poorer self-similarity of the GTBL flow. All of the terms have been nondimensionalized by $\Delta U^3/\delta_m$. The appropriateness of this normalization for the dissipation term has already been discussed (Sec. III A). The other terms are also best collapsed by this normalization, as expected for large-scale quantities.

If the mixing layer considered here were exactly self-similar, then the centerline level of $\overline{u_i u_j}/\Delta U^2$ would remain unchanged, implying that the time derivative (dashed) curves in Fig. 21 should be zero at $\xi=0$. This can be seen to be approximately the case; the discrepancy is a measure of departure from self-similarity. In fact, the $\overline{u_i u_j}$ profiles shown in Fig. 4 can be used together with the assumption of self-similarity to determine the $\partial \overline{u_i u_j}/\partial t$ profiles, which can then be compared to those in Fig. 21. Defining the functions f_{ij} and g_{ij} ,

$$f_{ij}(\xi) = \frac{\overline{u_i u_j}(\xi)}{\Delta U^2}, \quad g_{ij}(\xi) = \frac{\delta_m}{\Delta U^3} \frac{\partial \overline{u_i u_j}(\xi)}{\partial t}, \quad (A3)$$

and using the definition

$$\xi = \frac{x_2}{\delta_m(t)} \Rightarrow \frac{\partial \xi}{\partial t} = -\frac{\xi}{\delta_m} \frac{\partial \delta_m}{\partial t} = -r \xi \frac{\Delta U}{\delta_m}, \quad (A4)$$

where r is the growth rate defined in (6), it follows that

$$g_{ij} = \frac{\delta_m}{\Delta U} \frac{\partial f_{ij}}{\partial t} = \frac{\delta_m}{\Delta U} \frac{\partial f_{ij}}{\partial \xi} \frac{\partial \xi}{\partial t} = -r \xi f'_{ij}(\xi). \quad (A5)$$

As noted above, $g_{ij}(0)=0$. The agreement of the profiles predicted by this equation with those determined directly from the simulation (shown in Fig. 21) is quite good, with the maximum discrepancy being typically no larger than the discrepancy near $\xi=0$.

¹H. W. Liepmann and J. Laufer, "Investigations of free turbulent mixing," NACA Tech. Note TN 1257 (1947).

²I. Wygnanski and H. E. Fiedler, "The two-dimensional mixing region," J. Fluid Mech. **41**, 327 (1970).

³B. W. Spencer and B. G. Jones, "Statistical investigation of pressure and velocity fields in the turbulent two-stream mixing layer," AIAA Paper No. 71-613, 1971.

⁴R. G. Batt, "Turbulent mixing of passive and chemically reacting species in a low-speed shear layer," J. Fluid Mech. **82**, 53 (1977).

⁵J. H. Bell and R. D. Mehta, "Development of a two-stream mixing layer from tripped and untripped boundary layers," AIAA J. **28**, 2034 (1990).

⁶G. N. Abramovich, *The Theory of Turbulent Jets* (MIT Press, Cambridge, MA, 1963).

⁷C. M. Sabin, "An analytical and experimental study of the plane, incompressible, turbulent free-shear layer with arbitrary velocity ratio and pressure gradient," Trans. ASME D **87**, 421 (1965).

⁸G. L. Brown and A. Roshko, "On density effects and large structure in turbulent mixing layers," J. Fluid Mech. **64**, 775 (1974).

⁹P. E. Dimotakis and G. L. Brown, "The mixing layer at high Reynolds number: large-structure dynamics and entrainment," J. Fluid Mech. **78**, 535 (1976).

- ¹⁰C.-M. Ho and P. Huerre, "Perturbed free shear layers," *Annu. Rev. Fluid Mech.* **16**, 365 (1984).
- ¹¹C. Chandrsuda, R. D. Mehta, A. D. Weir, and P. Bradshaw, "Effect of free-stream turbulence on large structure in turbulent mixing layers," *J. Fluid Mech.* **85**, 693 (1978).
- ¹²P. Comte, M. Lesieur, and E. Lamballais, "Large- and small-scale stirring of vorticity and a passive scalar in a 3-D temporal mixing layer," *Phys. Fluids A* **4**, 2761 (1992).
- ¹³S. S. Collis, S. K. Lele, R. D. Moser, and M. M. Rogers, "The evolution of a plane mixing layer with spanwise nonuniform forcing," *Phys. Fluids* **6**, 381 (1994).
- ¹⁴K. J. Nygaard and A. Glezer, "Evolution of streamwise vortices and generation of small-scale motion in a plane mixing layer," AIAA Technical Report No. 91-0625, 1991.
- ¹⁵A. K. M. F. Hussain, "Coherent structures—reality and myth," *Phys. Fluids* **26**, 2816 (1983).
- ¹⁶R. E. Kelly, "On the stability of an inviscid shear layer which is periodic in space and time," *J. Fluid Mech.* **27**, 657 (1967).
- ¹⁷R. T. Pierrehumbert and S. E. Widnall, "The two- and three-dimensional instabilities of a spatially periodic shear layer," *J. Fluid Mech.* **114**, 59 (1982).
- ¹⁸G. M. Corcos and S. J. Lin, "The mixing layer: deterministic models of a turbulent flow. Part 2. The origin of the three-dimensional motion," *J. Fluid Mech.* **139**, 67 (1984).
- ¹⁹M. M. Rogers and R. D. Moser, "The three-dimensional evolution of a plane mixing layer: the Kelvin-Helmholtz rollup," *J. Fluid Mech.* **243**, 183 (1993).
- ²⁰R. Breidenthal, "Structure in turbulent mixing layers and wakes using a chemical reaction," *J. Fluid Mech.* **109**, 1 (1981).
- ²¹J. Jimenez, "A spanwise structure in the plane shear layer," *J. Fluid Mech.* **132**, 319 (1983).
- ²²L. P. Bernal and A. Roshko, "Streamwise vortex structure in plane mixing layers," *J. Fluid Mech.* **170**, 499 (1986).
- ²³J. H. Konrad, "An experimental investigation of mixing in two-dimensional turbulent shear flows with applications to diffusion-limited chemical reactions," Technical Report No. CIT-8-PU, California Institute of Technology, Pasadena, CA, 1976.
- ²⁴M. G. Mungal and P. E. Dimotakis, "Mixing and combustion with low heat release in a turbulent shear layer," *J. Fluid Mech.* **148**, 349 (1984).
- ²⁵M. M. Koochesfahani and P. E. Dimotakis, "Mixing and chemical reactions in a turbulent liquid mixing layer," *J. Fluid Mech.* **170**, 83 (1986).
- ²⁶S. M. Masutani and C. T. Bowman, "The structure of a chemically reacting plane mixing layer," *J. Fluid Mech.* **172**, 93 (1986).
- ²⁷J. C. Buell and N. N. Mansour, "Asymmetric effects in three-dimensional spatially-developing mixing layers," in *Proceedings of the Seventh Symposium on Turbulent Shear Flows* (Stanford University, Stanford, CA, 1989), p. 9.2.1.
- ²⁸P. S. Karasso and M. G. Mungal, "LIF measurements of mixing in turbulent shear layers," in *Proceedings of the Sixth International Symposium on Applications of Laser Techniques to Fluid Mechanics*, Lisbon, Portugal, 1992.
- ²⁹M. M. Rogers, R. D. Moser, and J. C. Buell, "A direct comparison of spatially and temporally evolving mixing layers," *Bull. Am. Phys. Soc.* **35**, 2294 (1990).
- ³⁰R. D. Moser and M. M. Rogers, "The three-dimensional evolution of a plane mixing layer: pairing and transition to turbulence," *J. Fluid Mech.* **247**, 275 (1993).
- ³¹P. R. Spalart, R. D. Moser, and M. M. Rogers, "Spectral methods for the Navier-Stokes equations with one infinite and two periodic directions," *J. Comput. Phys.* **96**, 297 (1991).
- ³²P. R. Spalart, "Direct simulation of a turbulent boundary layer up to $Re_\theta = 1410$," *J. Fluid Mech.* **187**, 61 (1988).
- ³³A. A. Townsend, *Structure of Turbulent Shear Flow* (Cambridge University Press, Cambridge, England, 1976).
- ³⁴J.-L. Balint and J. M. Wallace, "The statistical properties of the vorticity field of a two-stream turbulent mixing layer," in *Advances in Turbulence 2*, edited by H. H. Hernholz and H. E. Fiedler (Springer-Verlag, Berlin, 1989).
- ³⁵J. M. Bruns, R. C. Haw, and J. F. Foss, "The velocity and transverse vorticity field in a single stream shear layer," in *Proceedings of the Eighth Symposium on Turbulent Shear Flows* (Technical University of Munich, Germany, 1991), p. 3.1.1.
- ³⁶M. M. Rogers and P. Moin, "The structure of the vorticity field in homogeneous turbulent flows," *J. Fluid Mech.* **176**, 33 (1987).
- ³⁷J. M. Wallace (private communication, 1993).
- ³⁸P. E. Dimotakis, "Turbulent free shear layer mixing and combustion," in *High-speed-Flight Propulsion Systems*, in Progress in Astronautics and Aeronautics, edited by S. N. B. Murthy and E. T. Curran (American Institute of Aeronautics Astronautics, Washington, D.C., 1991), No. 137, pp. 265-340.
- ³⁹A. K. M. F. Hussain and K. M. B. Q. Zaman, "An experimental study of organized motions in the turbulent plane mixing layer," *J. Fluid Mech.* **159**, 85 (1985).
- ⁴⁰R. D. Mehta and R. V. Westphal, NASA Technical Report No. TM86698, 1985.
- ⁴¹J. C. Lasheras, J. S. Cho, and T. Maxworthy, "On the origin and evolution of streamwise vortical structures in a plane, free shear layer," *J. Fluid Mech.* **172**, 231 (1986).
- ⁴²R. D. Moser and M. M. Rogers, "Coherent structures in a simulated turbulent mixing layers," Technical Report No. TM103980, NASA (1992).
- ⁴³C. D. Winant and F. K. Browand, "Vortex pairing: the mechanism of turbulent mixing layer growth at moderate Reynolds number," *J. Fluid Mech.* **63**, 237 (1974).
- ⁴⁴D. W. Moore and P. G. Saffman, "The density of organized vortices in a turbulent mixing layer," *J. Fluid Mech.* **69**, 465 (1975).
- ⁴⁵J. Jimenez, "Kinematic alignment effects in turbulent flows," *Phys. Fluids A* **4**, 652 (1992).
- ⁴⁶R. W. Metcalfe, A. K. M. F. Hussain, S. Menon, and M. Hayakawa, "Coherent structures in a turbulent mixing layer: A comparison between direct numerical simulation and experiments," in *Turbulent Shear Flows 5*, edited by F. Durst, B. E. Launder, J. L. Lumley, F. W. Schmidt, and J. H. Whitelaw (Springer-Verlag, Berlin, 1987), pp. 110-123.
- ⁴⁷E. J. Broadwell and R. E. Breidenthal, "A simple model of mixing and chemical reaction in a turbulent shear layer," *J. Fluid Mech.* **125**, 397 (1982).
- ⁴⁸L.-S. Huang and C.-M. Ho, "Small-scale transition in a plane mixing layer," *J. Fluid Mech.* **210**, 475 (1990).
- ⁴⁹R. D. Moser and M. M. Rogers, "Mixing transition and the cascade to small scales in a plane mixing layer," *Phys. Fluids A* **3**, 1128 (1991).
- ⁵⁰J. Jimenez, M. Cogollos, and L. P. Bernal, "A perspective view of the plane mixing layer," *J. Fluid Mech.* **152**, 125 (1985).
- ⁵¹L. P. Bernal, "The coherent structure of turbulent mixing layers I. Similarity of the primary vortex structure. II. Secondary streamwise vortex structure," Ph.D. thesis, Caltech, 1981.
- ⁵²F. K. Browand and P. D. Weidman, "Large scales in the developing mixing layer," *J. Fluid Mech.* **76**, 127 (1976).
- ⁵³K. Shariff (private communication, 1993).

